A Study of Jet Response in the DØ Calorimeters

Master's Thesis in

Engineering Physics at

Lund Institute of Technology

by

Dag Gillberg

Supervisors:

Dugan O'Neil, Dept. of Physics, Simon Fraser University, Canada

Paula Eerola, Experimental Particle Physics, Lund University

Examiner:

Per Kristiansson, Division of Nuclear Physics, Lund Institute of Technology

December, 2004

Abstract

The Tevatron, situated at the Fermi National Accelerator Laboratory, is currently the world's highest energy collider with a centre of mass energy of 1.96 TeV. Protons and anti-protons are accelerated to velocities very close to the speed of light and collide in the centre of the DØ detector where the collision products are studied.

There are several very interesting physics processes that take place at these high energies. If we can measure the collision products precisely, we can reconstruct the underlying physics of the collision and get a better understanding of how the world works at the smallest scales.

The most usual decay products created in the proton-anti-proton collisions are sprays of particles called "jets". Understanding the energy calibration of these jets is therefore crucial for many high energy physics analyses at DØ.

The most important part of the jet energy calibration is the *jet response* — the fraction of the measured jet energy over the true jet energy. In this thesis, the jet response was determined from the transverse momentum imbalance in collisions where a photon is produced back-to-back with a jet. It was measured as a function of the jet energy in different parts of the DØ calorimeter.

Special attention was paid to jets with low transverse energies (up to ~ 25 GeV), for which the response has never been measured before by the DØ collaboration. By lowering the minimum jet transverse energy in the jet reconstruction algorithm, new jets with low energies were found that would not have been reconstructed using the standard settings. Including these jets in the measurement made it possible to detmine the jet response down to ~ 12 GeV.

Contents

1 Theoretical Introduction **1**

1.1 The Standard Model 1

1.2 Jet Production 2

2 Experimental Setup **4**

2.1 The Tevatron 4

2.2 The DØ Detector 5

2.2.1 The DØ Coordinate System 5

2.2.2 The Central Tracking 6

2.2.3 Preshowers 7

2.2.4 The DØ Calorimeters 7

2.2.5 Muon system 8

3 Introduction to Jet Energy Scale **10**

3.1 Calorimeter Response 11

3.2 Simple Model of a Jet 12

3.3 Jet Definition 13

3.4 Jet Energy Scale 16

3.5 Jet Response 17

3.6 Resolution Bias 19

3.7 The Energy Estimator 22

3.8 Low E_T Bias 24

4 Selection of $\gamma + jet$ Events **27**

4.1 Data Sample 27

4.2 Pre-selection 28

4.3 Event Selection 29

4.3.1 Bad Run Removal 29
4.3.2 Trigger Selection 29
4.3.3 Jet Selection 31
4.3.4 Photon Selection 32
4.3.5 Bad Jet Removal 32
4.3.6 Back-to-back Selection 33
4.3.7 Vertex Criteria 34
4.3.8 Cryostat Division 34
4.3.9 Selection Summary 35

5 Jet Response Measurement **36**
5.1 Energy Dependence 36
5.2 Cryostat Correction 46
5.3 Fitting Procedure 46
5.3.1 Result 47
5.3.2 Result Comparison 48
5.3.3 Low E_T Improvements 51

6 Systematic Error Estimation **53**
6.1 Jet Threshold Systematics 53
6.2 Photon Selection Systematics 59
H-Matrix 7 Systematics 59
Photon η Systematics 63
6.3 Back-to-Back Systematics 66

7 Summary **69**
References 71

Chapter 1

Theoretical Introduction

Since ancient times, two of the questions that have intrigued humanity are: "What is the world made of?" and "What holds it together?". Throughout history, scientists have attempted to answer these questions. As our knowledge of physics has improved, the particles regarded as fundamental have changed. The current model describing the elementary particles and their interactions is referred to as the "Standard Model" of Particle Physics.

1.1 The Standard Model

According to the Standard Model, the fundamental particles are classified as *quarks*, *leptons* and *gauge bosons*. The quarks and leptons constitute the building blocks of matter, and the gauge bosons mediate the forces between them.

There are six kinds of quarks and equally as many kinds of leptons. The most common lepton is the electron, which was discovered by J.J. Thomson over a century ago. The electron has two heavier cousins: the muon and the tau lepton. These are unstable and decay quickly under normal circumstances. The electron, muon and the tau lepton all have a negative electric charge and can interact electromagnetically through the exchange of photons (γ). The electromagnetic interaction is well described by the *Quantum Electrodynamics* (QED), which is one of the theories that the Standard Model is based upon. There are also three uncharged leptons that interact very weakly with other particles. These are called the electron, muon and tau neutrinos.

The quarks have an electromagnetic charge equal to $\pm 1/3$ or $\pm 2/3$ of the elementary charge and hence also experience the electromagnetic interaction. The quarks are however also subject to another kind of interaction that does not affect leptons — the *strong*

interaction. Due to the nature of this strong force, quarks are not observed as individual particles, but only as *hadrons* — particles consisting of several quarks bound together. Our two most familiar hadrons are the system of two up quarks and one down quark in its ground state, known as a proton, and the system of one up quark and two down quark in its ground state, which is a neutron. The strong force is carried by gluons (g) and is described by *Quantum Chromodynamics* (QCD), which just like QED, is part of the Standard Model.

There is also another force that acts on all quarks and leptons called the *weak interaction*. This force is transmitted by the massive W^+, W^- and Z^0 intermediate vector bosons and has a short range. A theory that unifies the electromagnetic and the weak interaction was developed by Glashow, Salam and Weinberg in the 1960s. This theory has been very successful, and the electromagnetic and weak interactions are commonly referred to as the *electroweak interaction*. However, this unification is only clearly appreciable at very high energies, at lower energies weak and electromagnetic interactions can still be clearly separated.

In the same way as photons mediate the electromagnetic interaction between particles with electromagnetic charge, gluons mediate the strong interaction between particles with *colour charge*. All quarks, but also gluons themselves, have colour charge. The fact that gluons have colour charge and hence can interact with other gluons makes the strong interaction quite different from the electromagnetic interaction. A property that follows from the gluon-gluon coupling is *asymptotic freedom*, which means that the strong interaction is weak at short distances, but gets stronger as the distance between colour charged particles increases.

1.2 Jet Production

The quarks inside a hadron interact frequently through emitting and absorbing gluons. If a quark (or gluon) within a hadron is pulled away (as might be the result in the case of a hadron-hadron collision), the energy of the strong field may become large enough to create a quark-antiquark pair. As a result, the quark (or gluon) will be emitted and undergo a complicated process that will result in a stream of collinear hadrons (mainly pions) with a total momentum close to the momentum of the emitted parton. Such an object is called a *jet*, and is what is observed in the detector.

The evolution of a jet is illustrated in Figure 1.1. The left picture depicts a *parton level jet*. A *parton* is a common name for a quark or a gluon. A parton that has not yet undergone fragmentation is sometimes referred to as a parton level jet.

A moving parton is a moving colour charge, and will radiate gluons and create quark-antiquark pairs. This process is called *fragmentation*, and the resulting spray of partons is usually referred to as a *parton cascade*. The coloured particles within such a cascade are combined into colourless hadrons through a process called *hadronization*. The shower of produced hadrons is usually referred to as a *particle level jet*.

Particle level jets produced from a given type of partons might vary widely in shape and particle content. When we try to measure a jet in a calorimeter there is also substantial blurring due to finite energy resolution and calorimeter cell granularity. Some particles of the jet may also escape undetected, for instance neutrinos or particles passing trough uninstrumented regions. This means that not all the energy of the jet will be measured in the calorimeter. A jet reconstructed from the energy deposited in a calorimeter by a particle level jet is referred to as a *calorimeter level jet*.

This study involves calibrating calorimeter level jets so that we can accurately reconstruct the energy of the particle level jets.

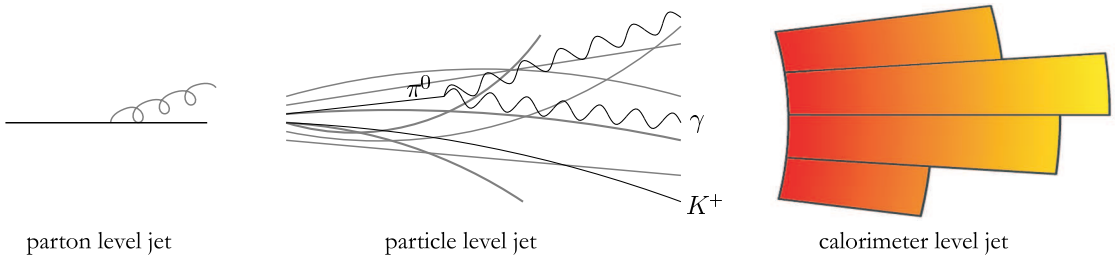

Figure 1.1: A parton (quark) radiates a gluon before hadronizing into a jet

Chapter 2

Experimental Setup

2.1 The Tevatron

The Tevatron, situated at the Fermi National Accelerator Laboratory near Chicago, is currently the world's highest energy collider, with a centre of mass energy of 1.96 TeV. It is a circular accelerator in which protons (p) and anti-protons ($\overline{p}$) circulate in opposite directions and are brought together into collision at two points in the B0 and D0 experimental areas. In these areas, two general purpose detectors, CDF and DØ respectively, measure the collision products.

An aerial view of Fermilab showing the accelerator facilities can be seen in Figure 2.1. A 400 MeV hydrogen ion (H^-) beam is produced from hydrogen, accelerated by a Cockroft-Walton accelerator followed by a 165 m linear accelerator. The electrons are stripped off as the ions pass through a carbon fiber foil into the Booster synchrotron ring. Here the produced protons are accelerated to 8 GeV before being transferred to the Main Injector where the particles are accelerated to 150 GeV. The Main Injector arranges the protons into a bunch structure before delivering them to the Tevatron where the proton bunches are finally accelerated to 980 GeV.

Proton bunches from the Main Injector are also used to produce anti-protons. A proton beam of 120 GeV is directed at a nickel/copper target. The anti-protons produced are accelerated to 8 GeV and accumulated. Once the number of anti-protons is sufficiently large, the anti-protons are passed to the Main Injector where they are accelerated to 150 GeV for transfer into the Tevatron.

36 bunches of protons and equally many bunches of anti-protons are delivered to the Tevatron with a 396 ns bunch spacing. The 36 bunches in each beam are organized into

Figure 2.1: Aerial view of Fermilab National Accelerator Laboratory showing some of the facilities described in Section 2.1.

three super-bunches, separated by a 2 μs gap. The beams are focused at the collision points, and $p\overline{p}$ collisions occur during the bunch-crossings.

The Tevatron is scheduled to run until 2009 delivering between 4 and 8 fb^{-1} to each of CDF and DØ. This provides an opportunity to study a wide variety of physics processes to unprecedented precision.

2.2 The DØ Detector

A sketch of the DØ detector is shown in Figure 2.2. The detector consists of four major components. Starting from the interaction point and moving outward, these are: The central tracking, the preshowers, the calorimeters and the muon system.

2.2.1 The DØ Coordinate System

The DØ coordinate system is a right-handed Cartesian system with origin in the geometric centre of the detector. The x-axis lies in the horizontal plane pointing outwards from the centre of the Tevatron ring, the y-axis points straight up, and the z-axis is pointing along the beam pipe in the direction of the outgoing proton beam.

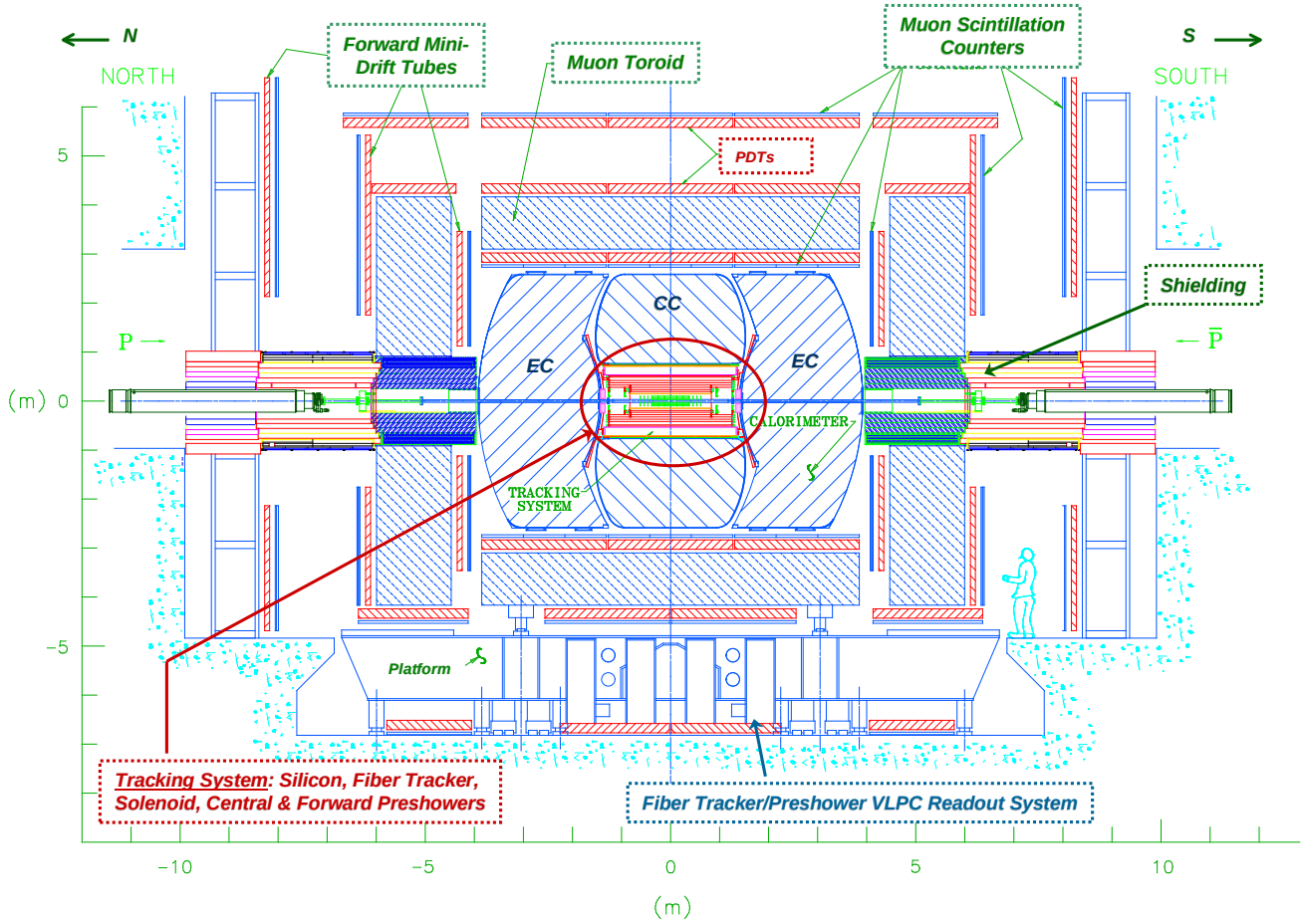

Figure 2.2: A cross section view of the DØ detector.

Since the protons and anti-protons are coming in along the z-axis, the (x, y)-plane is usually referred to as the transverse plane. The azimuthal angle ϕ of a vector (x, y, z) is the angle between the positive x-axis and the transverse component of the vector. The polar angle θ is defined as arccot z/r where $r = \sqrt{x^2 + y^2}$, but usually the pseudorapidity, $\eta = -\ln(\tan\theta/2)$, is used instead.

2.2.2 The Central Tracking

The central tracking system is built inside a 2 Tesla solenoid magnet with a mean radius of 60 cm. This will bend the paths of charge particles, and from the curvature of their tracks, their momenta can be calculated. The central tracking system consists of two tracking detectors: a silicon microstrip tracker (SMT) surrounded by the central scintillating fiber tracker (CFT).

2.2.3 Preshowers

The central and forward preshower detectors are placed before the calorimeters. They consist of lead radiators combined with scintillating material and are designed to identify and measure energy of particles that interact "too early" with matter in front of the calorimeter, *e.g.* the tracking material or the magnet.

2.2.4 The DØ Calorimeters

The DØ calorimeters are used to identify and measure the energy and direction of electrons, photons, jets, muons and missing transverse energy $\not\!\!E_T$. There are three cryostats with nearly equal size, the central calorimeter (CC) and the two endcap calorimeters (EC). Each calorimeter is divided in layers: innermost there are four electromagnetic (EM) layers, followed by the fine hadronic (FH) layers and the coarse hadronic (CH) layers.

The design of the EM layers is optimized for measurement of EM showers produced by electrons and photons. The third EM layer has increased granularity since this is where maximum shower development is expected. Most EM showers will not penetrate into the hadronic calorimeter, which is designed for good measurement of hadronic showers. Muons only deposit a small amount of energy in the calorimeter, and neutrinos no energy at all. Some energy will also be deposited in poorly instrumented regions and hence give no or little signal. This absence of measured energy results in a momentum imbalance in the transverse plane. This imbalance is called the missing transverse energy, $\not\!\!E_T$.

The basic unit of the DØ calorimeters is a calorimeter unit cell. Such a cell consists of an absorber plate (U, Cu or Fe) followed by a gap filled with liquid argon. In the middle of this gap is a G-10 board, with a 2.0 – 2.5 kV potential with respect to the grounded absorber plate. This potential difference induces a drift field across the liquid argon. As an incoming particle interacts with the dense matter in the absorber plate, a shower of secondary particles is produced. As they pass through the liquid argon, they ionize argon atoms, and negative charge will drift towards the signal boards. This results in a signal proportional to the energy loss of the incoming particle. A schematic view of two typical calorimeter unit cells is given in Figure 2.2.4. Several unit cells stacked on top of each other are read out together. Such a collection of unit cells are referred to as a "readout cell". In the rest of this thesis, "calorimeter cell" means readout cell and not unit cell.

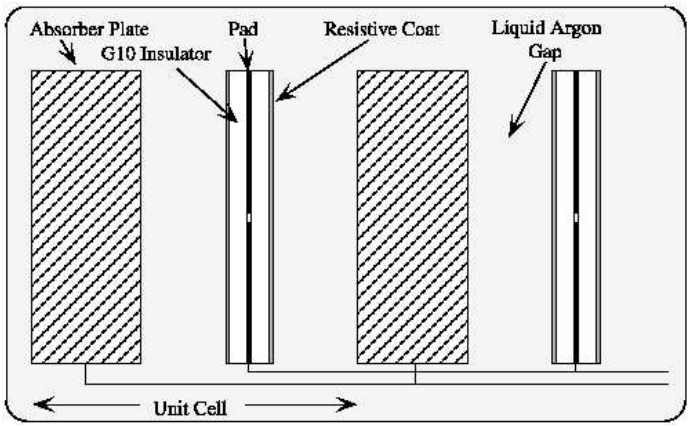

Figure 2.3: Drawing of two calorimeter unit cells. This figure was taken from [1] (Figure 3.8).

Figure 2.4 shows a side view of the calorimeters. We can see the layer structure, but also that cells with the same η (and ϕ) are arranged in "pointing towers", *i.e.* the towers point in towards the centre of the detector (the interaction point). Cells have a size of about $\Delta\eta \times \Delta\phi = 0.1 \times 0.1$ except in the third EM layer where the granularity is doubled.

2.2.5 Muon system

The DØ detector has a large muon system outside the calorimeter as can be seen in Figure 2.2. The muon detection strategy relies on the penetration power of muons since they do not undergo hadronic interactions but lose energy only through ionization. Almost all hadrons will be absorbed by the dense materials in the calorimeter and the muon system, while muons generally will pass through it all. A charged particle that penetrates the muon system is therefore defined as a muon.

The muon system consists of the wide angle muon spectrometer (WAMUS) covering the central detector ($|\eta| < 1$), the forward angle muon spectrometer (FAMUS) covering $1 < |\eta| < 2$ and a solid-iron magnet with at field of 1.8 Tesla. WAMUS and FAMUS each consists of several layers of drift chambers and scintillators where muons are detected. Due to the magnetic field, the path of the muons will be curved, and the muon momentum and charge are determined from the curvature of the tracks. These measurements can be improved by using additional information from the central tracking and the calorimeters.

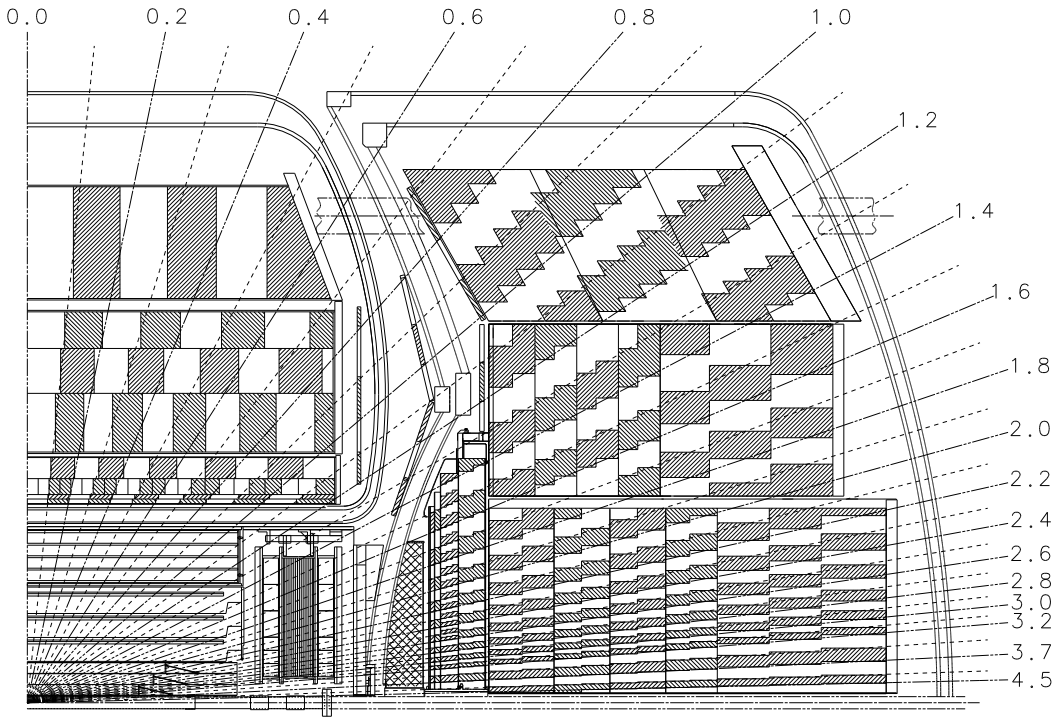

Figure 2.4: Side view of a quarter of the DØ calorimeters. The lines with numbers are lines of constant η. Cells are arranged into pointing towers along these lines. There are four EM layers in all cryostats, three FH layers in the CC and four in the ECs, and one CH layer in the CC and three in the ECs.

Chapter 3

Introduction to Jet Energy Scale

It is not easy to associate the measured jet energy in the calorimeter with the true underlying energy of the jet. Jets can show very different behaviours depending on what happens in the early stage of the hadronization process. For example, early radiated gluons may, or may not, be interpreted as separate jets, and if the leading particle created is a π^0 decaying to photons, the jet might look very much like an electromagnetic object. An illustration of the evolution of a jet is given in Figure 3.1.

Today, the Jet Energy Scale (JES) uncertainty is the dominant systematic error for several analyses at DØ such as top quark measurements and QCD precision tests. The dominant part of this uncertainty comes from the jet response in the calorimeter. The jet response error is especially large for jets with E_T below 25 GeV since the response measurements of these jets are biased due to the jet reconstruction threshold. Until now, the jet response in this low E_T region has been obtained through extrapolation from the unbiased data points at higher jet energies, which is the main reason for the large uncertainties.

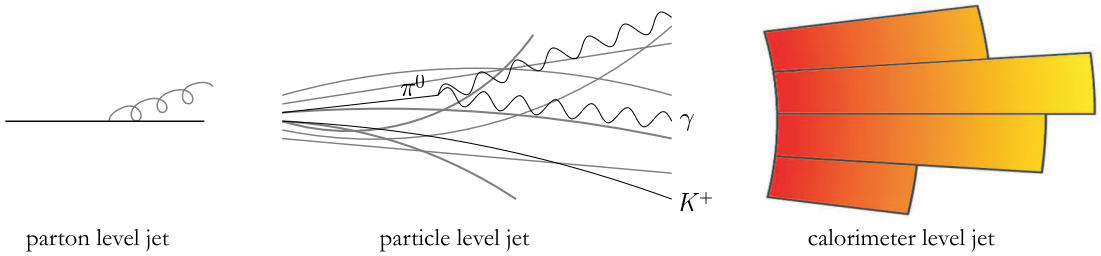

Figure 3.1: A parton (quark) radiates a gluon before hadronizing into a jet

One set of analyses that would benefit from a more precise jet response at low E_T is the study of top quark events. The lowest energy jets in top pair events are often between 15 and 25 GeV and hence in the region of large errors. As more data are recorded, statistical errors decrease and the JES precision becomes even more important in order to reduce the total uncertainty of the measurements.

In this study, we are extending the jet response measurement to low E_T by lowering the jet reconstruction threshold, which by far is the dominant source of bias at low E_T. The response measurement is done much in the same way as in earlier studies [2, 3, 4, 5].

3.1 Calorimeter Response

The DØ calorimeters were designed to be compensating, *i.e.* the calorimeter response of particles only interacting electromagnetically (R_{em}) is the same as the response of particles interacting purely hadronically via nuclear reactions (R_h). A perfectly compensating calorimeter will hence have $R_{em} = R_h$, which usually is written $e/h = 1$. The electromagnetic response can be studied since most electromagnetically interacting particles (*i.e.* photons, electrons or positrons) deposit all their energy in the EM section of the calorimeter. The purely hadronic response can, however, not be measured directly since hadronic showers have an electromagnetic fraction f_{em}, which shows large event-to-event fluctuations and, on average, tend to increase logarithmically with energy.

Significant attention was spent on calibrating the DØ calorimeters based on test beam data. Electron and charged pion beams were used, and good linearity between the measured signals and the incoming particle energy was achieved [6]. The response fraction $e/\pi^{\pm}$ was found to be close to unity, but greater than 1 and energy dependent. The pion response can be written as

$$R_{\pi^{\pm}} = f_{em} R_{em} + f_{had} R_h. \tag{3.1}$$

Using the relation $f_{em} + f_{had} = 1$ we can rewrite the above on the form

$$R_{\pi^{\pm}} = R_h + (R_{em} - R_h) f_{em}. \tag{3.2}$$

The electromagnetic fraction f_{em} of the shower has been parameterized by Wigmans [7,8] as

$$f_{em} = \alpha \ln \frac{E_{\pi^{\pm}}}{E_h}, \tag{3.3}$$

where α is assumed to be a constant, and the scale energy E_h of the hadronic shower is assumed to be 1 GeV for pion showers. Fits from test beam data gives $\alpha \approx 0.12$, but a closer look suggest that α is also weakly energy dependent [4]. A good fit is obtained using the logarithmic parameterization

$$\alpha = a_0 + a_1 \ln \frac{E_{\pi^\pm}}{E_h} \tag{3.4}$$

with $a_0 \approx 0.19$ and $a_1 \approx -0.016$. Combining Equations 3.2, 3.3 and 3.4 now allows us to express the energy dependence of the pion response in a form that fits the test beam data very well

$$R_{\pi^\pm} = b_0 + b_1 \ln \frac{E_{\pi^\pm}}{E_h} + b_2 \ln^2 \frac{E_{\pi^\pm}}{E_h}, \tag{3.5}$$

where the parameters $b_0 = R_h$, $b_1 = a_0(R_{em} - R_h)$ and $b_2 = a_1(R_{em} - R_h)$ are assumed to be constant as well as $E_h = 1$ GeV.

3.2 Simple Model of a Jet

In order to obtain an approximate prediction of the energy behaviour of the jet response, let us consider a simple model of a jet. An incident parton will fragment into hadrons as illustrated in Figure 3.1. Neutral pions and η mesons produced will decay into photons and give a purely electromagnetic response in the calorimeter. Charged hadrons will produce a hadronic shower on their own and give a response like $R_{\pi^\pm}$ described in Section 3.1. Assuming there are N_{π^0} electromagnetically interacting particles produced and $N_{\pi^\pm}$ charged hadrons having response $R_{\pi^\pm}$, allows us to write the jet response as

$$R_{jet} = \frac{1}{E_{jet}} \left(\sum_{N_{\pi^0}} R_{\pi^0}(E_i^{\pi^0}) \cdot E_i^{\pi^0} + \sum_{N_{\pi^\pm}} R_{\pi^\pm}(E_i^{\pi^\pm}) \cdot E_i^{\pi^\pm} \right) \tag{3.6}$$

where $E_i^{\pi^\pm}$ is the energy of charged hadron number i. The fraction of the jet energy carried by the electromagnetically interacting particles produced varies widely, but a typical value is 30% which is also consistent with the ratio of neutral particles [4]. A typical number of produced particles is 10.

If we assume that the incoming parton hadronizes to three π_0s and seven charged pions, each having the energy $E_{jet}/10$, we can now write the jet response as:

$$R_{jet} = 0.3R_{\pi^0}(0.1E_{jet}) + 0.7R_{\pi^\pm}(0.1E_{jet}) \tag{3.7}$$

Setting $R_{\pi^0} = R_{em}$ and $R_{\pi^\pm}$ according to Equation 3.5 and assuming R_{em} and R_h to be independent of energy gives us the following expression for the jet response:

$$R_{jet} = p_0 + p_1 \ln \frac{E_{jet}}{E_0} - p_2 \ln^2 \frac{E_{jet}}{E_0}, \tag{3.8}$$

where E_0 is an arbitrary energy constant and the parameters p_0 – p_2 are independent of energy.

The functional form of Equation 3.8 agrees well with the jet response measured in data, and is used to fit the data points in a given cryostat of the calorimeters (fit results are given in Figure 5.9).

It should be pointed out that there are important effects that have not been considered in the arguments given in this section. Examples are energy deposition in poorly instrumented regions and production of weakly interacting particles.

3.3 Jet Definition

As illustrated in Figure 3.1, the energies measured in the calorimeter cells are "footprints" of parton level jets. An ideal jet algorithm would search through the whole detector and identify all cells belonging to each jet in the event. Due to the complex nature of jets and computing limitations, it is not at all trivial to implement such an algorithm. The most common approach is to centre fixed-sized cones around (hadronic) energy clusters in the calorimeter and define a calorimeter level jet by the parameters of the cells within such a cone. The method used in this study is called the *Improved Legacy Cone Algorithm* (ILCA) or simply the *Run II Cone Algorithm* [9, 10].

The Run II Cone Algorithm uses full four-vector variables for all jet components. Objects, like calorimeter cells or pointing towers, are combined according to the so-called *E-Scheme* — their four-momenta are added — and the angular coordinates (Y, ϕ) or (η, ϕ) are calculated from the four-vector components:

$$\text{the azimuthal angle} \quad \phi = \arctan \tfrac{p_y}{p_x}, \tag{3.9}$$

$$\text{the rapidity} \quad Y = \tfrac{1}{2} \ln \tfrac{E+p_z}{E-p_z}, \tag{3.10}$$

$$\text{the polar angle} \quad \theta = \operatorname{arc\,cot} \tfrac{p_z}{p_T}, \tag{3.11}$$

$$\text{the pseudorapidity} \quad \eta = -\ln \tan \tfrac{\theta}{2}. \tag{3.12}$$

For computing time reasons, the calorimeter cells are first combined into pointing tower

objects. These are further combined into "preclusters" by the *Simple Cone Algorithm*. These are used as starting points (seeds) for the actual cone algorithm that uses an iterative process to find "stable cones"—*i.e.* the energy weighted centroid of all objects within the cone is aligned with the geometrical axis.

The three steps that describe the process from the cell energies to Run II jets are outlined below.

Step 1 – *From cells to towers*

Each calorimeter cell is considered a massless object and is assigned the four vector $(E_{cell}, \vec{p}_{cell})$, where E_{cell} is the measured energy and $\vec{p}_{cell}$ is a vector of magnitude $|E_{cell}|$ directed from the primary vertex to the centre of the cell. The following selection criteria are applied to the cells:

a. Each cell is required to have $|E_{cell}| > 2.5\ \sigma_{cell}$, where σ_{cell} is the measured energy width due to electronic noise.

b. Cells identified as hot cells by the NADA algorithm are removed [11].

c. If the T42 algorithm [12,13] is used, cells with energies due only to electronic noise are removed:
All cells with $E_{cell} > 4\ \sigma_{cell}$ are first selected. The neighbouring[1] cells to these 4 σ-cells are also kept if they have $E_{cell} > 2\ \sigma_{cell}$. After this selection only positive energy cells remain.

All surviving cells belonging to a given tower are combined into a tower object according to the *E-Scheme* described above. Towers with negative squared masses are removed.[2]

Step 2 – *From towers to preclusters using the Simple Cone Algorithm*

The Simple Cone Algorithm forms so-called "preclusters" through merging nearby towers. Preclusters are cones with radius 0.3 in (η, ϕ)-space. The size of a tower is approximately 0.1×0.1 in (η, ϕ)-space. A rough scheme of this algorithm is given below.

a. A p_T-sorted list of the towers is created.

[1] The "neighbouring" cells are defined as the eight surrounding cells in the same layer plus the nine in front and the nine behind, in analogy with "Rubik's cube"

[2] if the T42 algorithm is not applied, towers with small negative mass may be included (as long as $|\vec{p}| - |E| < 0.001$ GeV and $|E| > |p_z|$ is fulfilled)

b. If there are no towers with $p_T > 0.5$ GeV the algorithm terminates, otherwise the highest p_T tower is picked out from the list and is used to define a precluster P.

c. The highest p_T tower within $\Delta R = 0.3$ of P is removed from the list and is combined with P. This is repeated until no towers remain within 0.3 from P.

d. If P contains at least two towers and has $p_T > 1$ GeV, it is added to the final list of preclusters. The algorithm jumps back to step **b.** and continues through the scheme.

Step 3 – *From preclusters to Run II Cones*

The Run II Cone Algorithm uses the list of towers from Step 1 and the list of preclusters from Step 2 as inputs. The centres of the preclusters, but also the midpoints between pairs of preclusters, are used as the starting points (seeds) for this iterative algorithm. The stable cones found are first saved as "proto-jets." When this is done, overlapping proto-jets are either merged or split before declaring them as jets.

Three important parameters are:

- The radius of the cone $\mathcal{R}$ defined in (Y, ϕ)-space (0.5 in this study)
- `ET_Split_Frac`: overlapping proto-jets with shared energy fraction above the value of this parameter will be merged; if below they will be split. The default value is 50%.
- `Min_Jet_ET`: only jets with p_T above the value of this parameter will be stored. The default value is 8 GeV; 3 GeV was used in this study.

A description of the Run II Cone Algorithm is given below.

a. All towers with centres within $\mathcal{R}$ from the first seed are combined according to the *E-Scheme* into a "proto-jet candidate" PC. The (Y, ϕ)-coordinates of PC (obtained from equations 3.9 and 3.10) define the next centre point, and PC is redefined from the towers within $\mathcal{R}$ around this point. This is repeated until a stable cone is found (*i.e* the new cone contains the same towers as the previous one) or for a maximum of 50 times. The cone is added to a list of proto-jets.

b. The procedure above is repeated for all starting points, but to speed up the algorithm the iterations are cancelled if the centre point approaches a stable cone

that has already been found. The iterations are also cancelled if the p_T of PC at any time goes below 0.5 `Min_Jet_ET`. This results in a list of proto-jets without duplicates, which is sorted by decreasing p_T.

c. A loop is done over the list. If two proto-jets share at least one tower, the fraction "shared p_T" divided by the p_T of the lower p_T jet is calculated. If this fraction is greater than `ET_Split_Frac`, the proto-jets are merged (*i.e.* a new proto-jet defined by all their towers replaces the two), if the fraction is lower, each shared tower is assigned only to the proto-jet that is closest in (Y, ϕ)-space.

After these procedures, no proto-jets share any towers, and they are now stored as Run II jets.

3.4 Jet Energy Scale

The following relationship is used to obtain the particle level jet energy from the measured jet energy at DØ:

$$E_{jet}^{ptcl} = \frac{E_{jet}^{meas} - E_O(\mathcal{R}, \eta, \mathcal{L})}{R_{cone}(\mathcal{R}, E, \eta) R_{jet}(\mathcal{R}, E, \eta, \phi)} \tag{3.13}$$

- E_{jet}^{meas} is the measured jet energy, *i.e.* the sum of the tower energies within the cone assigned to the jet by the jet finding algorithm described in Section 3.3.

- $E_O(\mathcal{R}, \eta, \mathcal{L})$ is an offset due to background such as uranium noise and pile-up energy from previous interactions. This offset is calculated as the energy density multiplied by the angular area of the jet cone in (Y, ϕ)-space, $\pi\mathcal{R}^2$. The energy density also depends on η, the luminosity $\mathcal{L}$ and whether the noise-reducing T42 algorithm has been applied.

- $R_{cone}(\mathcal{R}, E, \eta)$ is the fraction of the jet energy that is inside the algorithm cone. This fraction depends on the size of the cone, η_{jet} and the jet energy.

- $R_{jet}(\mathcal{R}, E, \eta, \phi)$ is the jet response in the calorimeter and should only be dependent on the parameters of the true jet and the calorimeter. However, since we are using E_{jet}^{meas}, we will also see a jet algorithm dependence, and due to various detector effects we will also have a η_{jet} and ϕ_{jet} dependence.

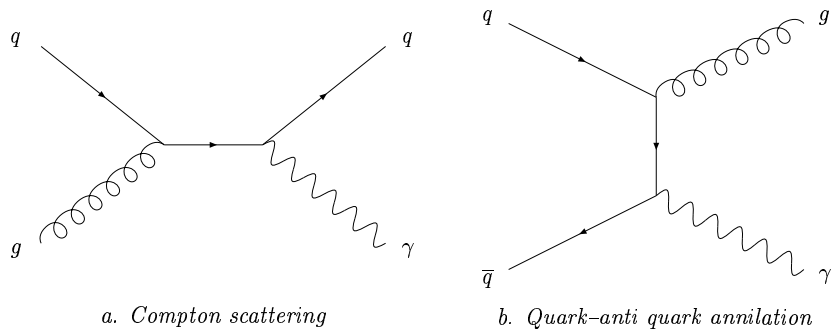

Figure 3.2: Feynmann diagrams of "direct photon" production.

3.5 Jet Response

At DØ, as well as in other experiments, the jet response (R_{jet}) is measured from p_T imbalance in $\gamma + jet$ events. The method is based on a two body process where the incoming partons produce a so-called "direct photon" and a jet (see Figure 3.2). Since the initial state partons are travelling along the beam line with negligible transverse momenta,[3] momentum conservation gives

$$\vec{p}_{T\gamma} + \vec{p}_{Tparton} = 0. \tag{3.14}$$

Neglecting hadronization effects, one can assume the total momentum of the produced hadrons to be very close in magnitude to the momentum of the final state photon. Hence with reasonable precision:

$$\vec{p}_{T\gamma} + \vec{p}_{Thad} = 0. \tag{3.15}$$

When measuring energy in a calorimeter we will get a transverse imbalance due to different hadronic and electromagnetic responses:

$$R_{em}\vec{p}_{T\gamma} + R_{had}\vec{p}_{Thad} = -\vec{\not{E}}_T. \tag{3.16}$$

Here R_{had} is the response of the hadronic recoil of the photon. This might consist of one or more jets. To a first approximation we would expect the electromagnetic response R_{em} to be equal to unity since the detector was calibrated from electron test beam data. However, an energy scale was needed after the detector was put together since a small

[3]The proton and the anti-proton are travelling along the beam line and will therefore have zero transverse momenta. The two interacting partons will, however, each have a small intrinsic transverse momenta k_T (since they can be considered moving within the proton/anti-proton). This intrinsic k_T is negligible in comparison with the p_Ts of the final state photon and jet [14].

shift of R_{em} was observed in the different calorimeter modules. This electromagnetic energy scale is known with good precision after studies of $Z \to e^+e^-$, $J/\psi \to e^+e^-$ and $\pi_0 \to \gamma\gamma$ events [15] (for Run I see [16, 17, 18]).

The missing transverse energy, $\not\!\!E_T$, is well measured in the DØ calorimeters due to the full angle coverage, fine segmentation and good energy resolution. The $\not\!\!E_T$ used in this study is calculated from the calorimeter towers with positive energy obtained in the same way as by the jet algorithm described in Step 1 of Section 3.3. The $\not\!\!E_T$ is calculated as the sum of the the transverse momentum components of all towers with positive energy:

$$\vec{\not\!\!E}_T = -\sum_{E_i>0}^{towers} \vec{p}_{Ti}. \tag{3.17}$$

The electromagnetic response correction to $p_{T\gamma}$ changes the energy content of some of the towers and necessitates a correction to $\not\!\!E_T$. By adding $(1 - R_{em})\vec{p}_{T\gamma}$ to both sides of Equation 3.16 we get

$$\vec{p}_{T\gamma} + R_{had}\vec{p}_{Thad} = -\vec{\not\!\!E}_T + (1 - R_{em})\vec{p}_{T\gamma}. \tag{3.18}$$

Since we know R_{em} we can correct the $\not\!\!E_T$ for the EM scale:

$$\vec{\not\!\!E}_T^{EMcorr} = \vec{\not\!\!E}_T - (1 - R_{em})\vec{p}_{T\gamma} \tag{3.19}$$

Using this quantity together with the relation $\vec{p}_{Thad} = -\vec{p}_{T\gamma}$ from Equation 3.15, allows us to express Equation 3.18 on the following form:

$$\vec{p}_{T\gamma} - R_{had}\vec{p}_{T\gamma} = -\vec{\not\!\!E}_T^{EMcorr} \tag{3.20}$$

By projecting the missing energy vector along the direction of the photon, we can now find an expression for hadronic response:

$$-\vec{n}_{T\gamma} \cdot \vec{\not\!\!E}_T^{EMcorr} = \vec{n}_{T\gamma} \cdot (\vec{p}_{T\gamma} - R_{had}\vec{p}_{T\gamma}) = p_{T\gamma} - R_{had}p_{T\gamma}$$

$$R_{had} = 1 + MPF = 1 + \frac{\vec{\not\!\!E}_T^{EMcorr} \cdot \vec{n}_{T\gamma}}{p_{T\gamma}}. \tag{3.21}$$

In the case of a two-body process, *i.e.* in the absence of initial or final state radiation, we have $R_{jet} = R_{had}$. Calculating the jet response in this way is called the Missing E_T Projection Fraction Method.

If there were no offset and showering effects (described in Section 3.4) then R_{jet} could simply be calculated in direct photon events as the measured transverse jet momentum

over the corrected photon p_T. The *MPF* is independent of the offset and showering effects since we expect the offset to be equal in all directions and hence cancel out when $\not{E}_T$ is calculated. Since the *MPF* does not depend on the jet algorithm, we do not need to worry about jet algorithm effects like R_{cone}.

Expressing the jet response in the form

$$R_{jet} \approx \frac{p_{Tjet}^{meas}}{p_{T\gamma}} \approx \frac{E_{Tjet}^{meas}}{E_{T\gamma}} = \frac{E_{jet}^{meas}}{E'} \tag{3.22}$$

is hence only an estimate, but this expression is often useful to quickly estimate the impact a certain bias will have on the jet response. The variable E' will be introduced in Section 3.7.

3.6 Resolution Bias

The examples and reasoning given in this section are based on Section 6.8 in [4].

As seen in Section 3.5, the jet response R_{jet} can be calculated using the Missing E_T Projection Fraction Method (Equation 3.21) in $\gamma + jet$ events. The most straight forward way to study the measured jet energy (E_{jet}^{meas}) dependence of this response would be to simply bin the events in E_{jet}^{meas} and look at the response in each bin. However, due to the poor resolution of the measured jet energy in combination with the rapidly falling photon cross section, this approach will severely bias our response measurement.

To illustrate this bias let us consider an ensemble of leading order $\gamma + jet$ events where the final state photon and parton are travelling back-to-back with $p_T = 40$ GeV. For simplicity, let us further assume that the parton is massless and $\eta_\gamma = \eta_{parton} = 0$ so that we have $p_T = E_T = E = 40$ GeV for both particles. The responses and the fractional resolutions are assigned the following reasonable values [2]:

$$\sigma/E = \sqrt{N^2/E^2 + S^2/E + C^2} \tag{3.23}$$

$$R_{em} = 1 \quad N_{em} = 0.39 \text{ GeV}, S_{em} = 0.135 \sqrt{\text{GeV}},\ C_{em} = 0.005 \tag{3.24}$$

$$R_{jet} = 0.8 \quad N_{jet} = 3.85 \text{ GeV}, S_{jet} = 0.54 \sqrt{\text{GeV}},\ C_{jet} = 0.03 \tag{3.25}$$

Under these circumstances, the measured jet and photon E_T will be distributed as shown in Figure 3.3. On average the jet will be measured 20% low at 32 GeV due to the jet response, but sometimes the measured jet energy might fluctuate to energies below

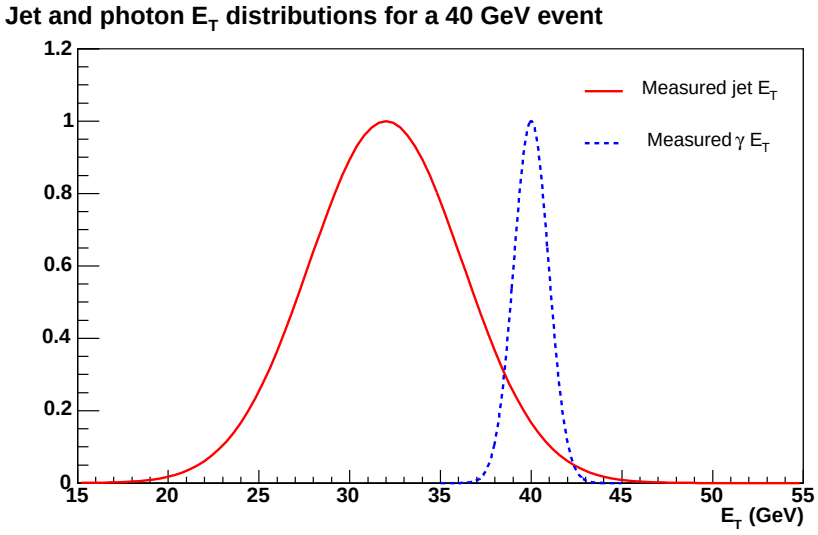

Figure 3.3: Distributions of the measured transverse energies of the photon and the jet in direct photon events where both the photon and the parton have $\eta = 0$ and $E_T = 40$ GeV.

25 GeV or above 40 GeV. The measured photon E_T is much closer to the parton E_T at 40 GeV.

If we instead consider an ensemble of direct photon events where the measured jet E_T is fixed at 32 GeV but with no constraints on the parton, we would get distributions like the ones shown in Figure 3.4. The E_T distributions of the parton and the photon are both wide, but it should be noted that their transverse energies still are close in magnitude in a given event due to the good electromagnetic resolution.

In Figure 3.4 we can see that most partons producing a jet which measures at 32 GeV in the calorimeter have an initial energy of around 40 GeV. This is what we expect since jets with true energies of 40 GeV should – on average – give a measured jet energy of $R_{jet}E_{jet} = 0.8 \cdot 40$ GeV $= 32$ GeV. The left tails of Figure 3.4 corresponds to lower-E_T-events where the jet fluctuates high. Here we see events where the parton E_T is as low as 30 GeV, *i.e.* jets with a true E_T of 30 GeV, that fluctuate high and will be measured at 32 GeV. We also see jets with E_T as high as 50 GeV that fluctuate low.

The arguments given above are based on the assumption that the underlying parton E_T can take any value with equal probability. If this was the case in data, we would (neglecting other possible effects) expect to see a photon E_T distribution similar to the

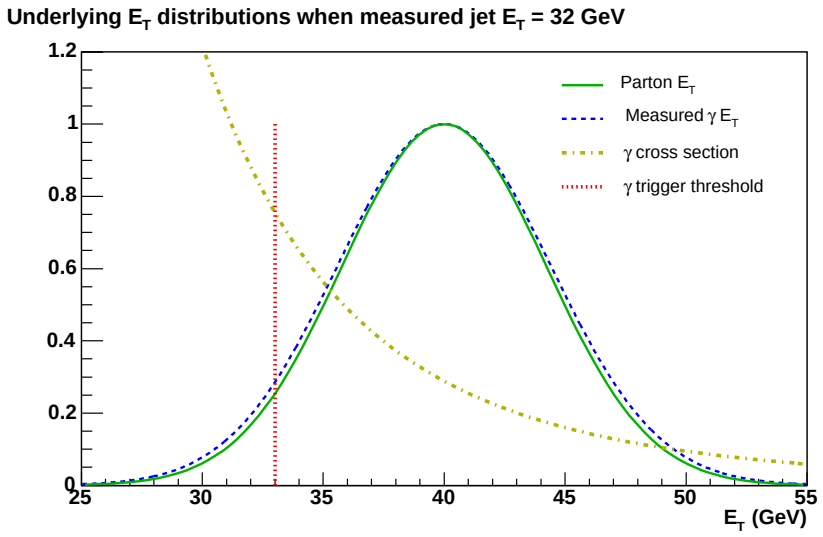

Figure 3.4: Distributions of the true parton E_T and the measured photon E_T in leading order $\gamma + jet$ events where $E_{Tjet}^{meas} = 32$ GeV.

one in Figure 3.4 in an E_{jet}^{meas}-bin centred at 32 GeV, and the jet response would be measured correctly. However, in real $\gamma + jet$ data these distributions, and hence also the jet response, are strongly biased mainly due to the following two effects:

a. The direct photon cross section falls rapidly with increasing E_T ($\approx$ as $E_{T\gamma}^{-5}$) as shown in Figure 3.4. This will skew our photon E_T distribution towards lower values as illustrated in Figure 3.5. In our E_{jet}^{meas}-bin centred at 32 GeV we will now have a surplus of low E_T events where the measured jet energy fluctuates high. The mean measured photon E_T falls from 40 to about 37.7 GeV, which means that the response will be measured at 0.849, 6.1% too high.

The falling cross section of direct photon production will hence bias our response measurement towards higher values. This effect can be seen clearly in Figure 3.6. The response measured in E_{jet}^{meas}-bins (white points) are higher than the unbiased measurement (black points).

b. Another bias arises due to EM trigger thresholds or other truncations of the photon E_T distributions. As illustrated in Figure 3.5, events with $E_{T\gamma}$ below the threshold (shown in Figure3.4) will be removed. Since the photon and parton transverse energies are close in magnitude this will result in less events with high response (low E_T events where the jet fluctuates high), and the response will be biased

towards lower values when approaching an EM threshold.

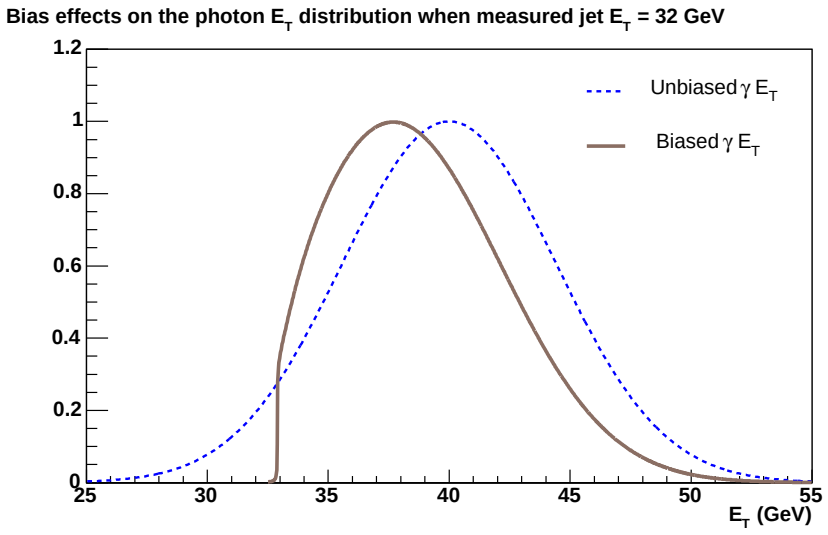

Figure 3.5: Illustration of the measured $E_{T\gamma}$ distributions in an E_{jet}^{meas}-bin before (dashed) and after (solid) the biases illustrated in Figure 3.4 are applied. The rapidly falling direct photon cross section pulls the photon E_T towards lower values giving a jet response measured too high. The trigger threshold truncates the $E_{T\gamma}$ distribution which biases the jet response measurement towards lower values.

3.7 The Energy Estimator

As first described in [19] there is a beautiful way to overcome the biases discussed in the previous section. The underlying jet energy can be estimated using Equation 3.15 and the relation $E = E_T \cosh \eta$ using only only well-measured variables:

$$E' = E_{T\gamma} \cosh \eta_{jet} \tag{3.26}$$

This quantity is called the *Energy Estimator* and is strongly correlated with the measured jet energy. Through binning the data in E', the jet resolution bias is removed since we now are dealing with the photon resolution, not the jet resolution. In order to express this unbiased response as a function of the measured jet energy, the mean jet response and the mean measured jet energy are determined individually in each E' bin and those values are plotted against each other.

This approach was simulated in [2], and the result is shown in Figure 3.6. One can clearly see that the measurement where R_{jet} is binned directly in E_{jet}^{meas} (white points) do not

agree with the true response (black line). The reason is the bias due to the rapidly falling direct photon cross section in combination with the jet resolution as described Step a of Section 3.6. Binning the response in E', and then mapping the response to the measured jet energy (black points) gives a measured response much closer to the true response. The jet reconstruction threshold was not considered in the simulation, and the low E_T bias is hence not shown in Figure 3.6.

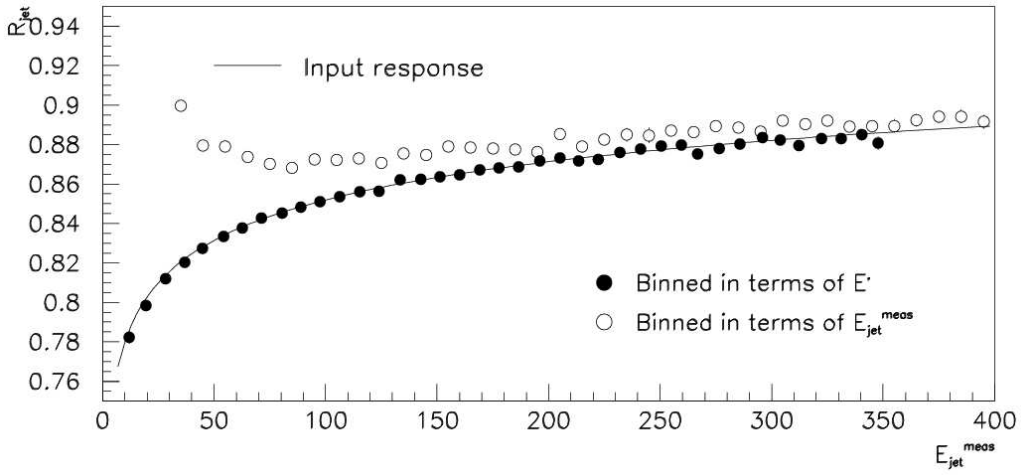

Figure 3.6: Simulation of a response measurement. Through binning the events in terms of E', one comes much closer to the true response. Binning directly in the measured jet energy gives a biased measurement. The low E_T bias is not illustrated. This figure is taken from [2] where it is Figure 3.7.

In a two-body $\gamma + jet$ event where the incoming partons have zero transverse momenta, E' will be equal to the true particle level jet energy if:

- η of the reconstructed jet is equal to η of the particle level jet
- $\vec{p}_{T ptcl} = \vec{p}_{T\gamma}$, implying that hadronization effects are neglected

The Energy Estimator is hence rather an estimate of the parton energy than the particle level jet energy.

3.8 Low E_T Bias

The introduction of E' was a major improvement for jet response measurements using the Missing E_T Projection Fraction Method. The bias due to photon p_T thresholds is removed since E' is expressed directly in $E_{T\gamma}$, and the bias due to the direct photon cross section is now strongly reduced.

However, using E' will also introduce a new bias at low E_T (not illustrated in Figure 3.6). Since we now are binning in terms of $p_{T\gamma}$, our response measurement will be sensitive to constraints on the jet p_T. In the same way that trigger thresholds might bias our response measurement through truncating the low E_T tail of the photon E_T distribution in an E_{jet}^{meas}-bin (as described in in Point **b.** of Section 3.6), the jet reconstruction threshold might bias the response through truncating the low p_T tail of the jet p_T distribution in an E'-bin. This pushes the mean measured jet energy towards higher values in a given E' bin, which results in a measured jet response that is too high (see Equation 3.22).

Since E' is an estimation of the parton level jet energy, we expect an E' bin centred at 40 GeV to have a jet p_T distribution similar to the one in Figure 3.3. We expect to see jets with p_T as low as 20 GeV, but no jets close to the standard jet p_T reconstruction threshold at 8 GeV. Here the jet response will be measured correctly. If we instead consider an E'-bin centred at 23 GeV, and assume the jet response is 0.65 for this energy, we would expect the jet p_T distribution to take the form of a Gaussian centred at $R_{jet}E' = 15$ GeV. Calculating the jet resolution for these jets according to Equation 3.23 (assuming all jets are in the CC with $\eta \approx 0$ so that $E_{jet}^{meas} \approx E_{Tjet}^{meas} \sim p_{jet}^{meas}$) gives the p_{Tjet} distribution shown in Figure 3.7. We can see that a significant part of the distribution is below the jet threshold at 8 GeV.

Due to inefficiencies in the jet reconstruction at low E_T, there will be events where jets with p_T above the threshold will not be found. An illustration of the jet reconstruction efficiency when using the standard jet reconstruction threshold at 8 GeV is shown in Figure 3.8. The efficiency does not reach 100% until the measured transverse momentum of the jet reaches about 15 GeV. This means that all jet p_T distributions where a significant part of the low p_T tail is below 15 GeV will be biased. Lowering the jet p_T reconstruction threshold will push the inefficiencies to lower p_T.

In Figure 3.7 the jet reconstruction efficiency is illustrated for two different jet p_T re-

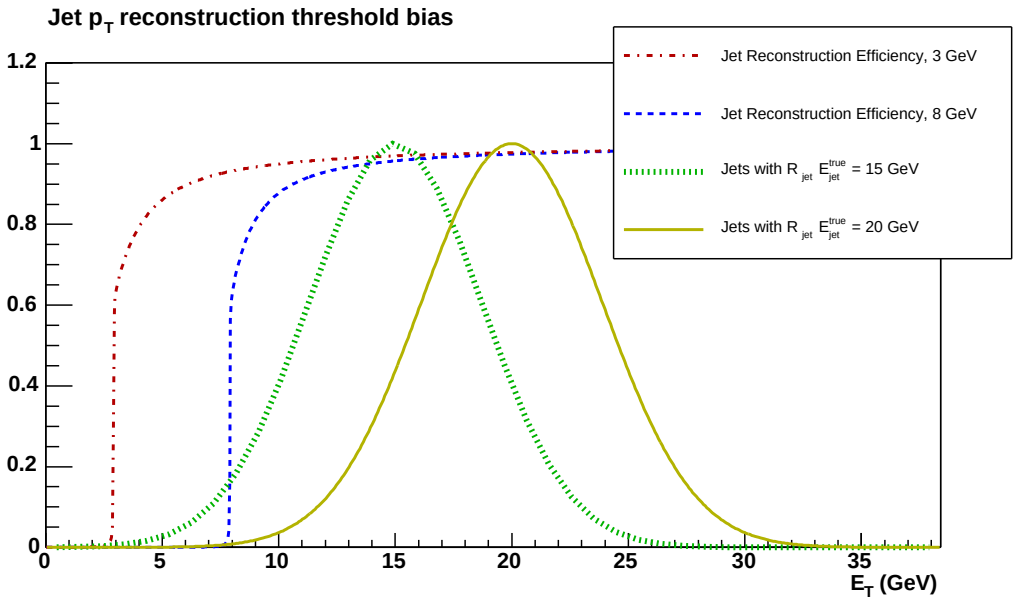

Figure 3.7: Illustration of the jet reconstruction efficiency using two different jet reconstruction thresholds. With the standard jet p_T threshold at 8 GeV the Run II Cone Algorithm reaches 100% efficiency at measured jet $E_T \sim 15$ GeV (blue dashed curve). With the threshold lowered to 3 GeV we expect to reach 100% efficiency at about 10 GeV (red point-dashed curve). Jets with measured E_{Tjet} ($= R_{jet}E_{Tjet}^{true}$) below about 20 GeV are in the region of inefficiency when the 8 GeV threshold is used.

construction thresholds: the standard one at 8 GeV, and the lowered one used in this study at 3 GeV. Two jet p_T distributions are shown, one centred at 15 GeV, and one at 20 GeV. These are assumed to come from two different E'-bins. The jet resolutions have been calculated using Equation 3.23.

The region of jet reconstruction inefficiencies using the 8 GeV reconstruction threshold reaches up to about 15 GeV. The jet p_T distribution centred at 15 GeV will hence be severely biased with this jet reconstruction threshold. The distribution centred at 20 GeV has some overlap with the region of inefficiency and experiences a weaker bias. E'-bins that have a jet p_T distribution centred above 20 GeV should not suffer from the jet reconstruction threshold bias.

Lowering the jet threshold to 3 GeV pushes the region of reconstruction inefficiency down to about 10 GeV, and E'-bins with mean jet p_T down to about 15 GeV will be measured correctly.

Systematic effects of lowering the jet threshold are discussed in Section 6.1.

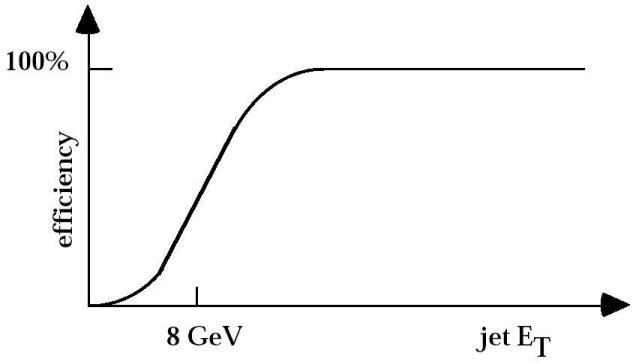

Figure 3.8: A jet clustering threshold at 8 GeV will result in jet reconstruction inefficiencies up to $\sim$ 15 GeV. This figure is taken from [4] (Figure 6.22).

Chapter 4

Selection of $\gamma + jet$ Events

To study the response, one ideally would like a sample of pure direct photon events evenly distributed over a large energy range in all parts of the detector. There are however many different physical processes where a jet and an electromagnetic object are produced (or mis-reconstructed), hence it is not trivial to obtain a pure direct photon sample.

The initial data sample used is a sample of "isolated photon" events, which means events that satisfied an isolated photon trigger. Thereafter, a set of selection criteria are applied to remove background and assure good quality of the events. These criteria are described below.

4.1 Data Sample

The data used for this study were recorded at DØ during the period April 2002 – August 2003. The data were reconstructed in various p14 releases and skimmed by the Common Sample Group [20]. The `JESB` skim was used which requires that an isolated photon trigger was fired and that at least one electromagnetic object was reconstructed with $p_T > 4$ GeV and EM ID = 10 or ± 11.[1] Information about the data skims used is given in Table 4.1.

[1] Electromagnetic objects found by the EM cluster algorithm will get EM ID 10 if there is no track match, 11 if the charge of the track is negative (electrons) and -11 if the charge is positive (positrons).

SAM Definition Name	N_{events}	Most data taken	Trigger list
`CSskim-JESB-all-p14.03-p14.fixtmb.01`	15.4 M	June – July 2003	v11/v12
`CSskim-JESB-p14.05.00-p14.fixtmb.02`	11.7 M	April - June 2003	v11
`CSskim-JESB-p14.05.02`	9.6 M	Jan 2003	v9/v10
`CSskim-JESB-p14.06.00`	4.1 M	Aug 2002	v8

Table 4.1: Data information. At least half of the data in each skim was taken during the time period given in the third column.

4.2 Pre-selection

The data were first processed using `top_analyze Stradivarius` [21]. The built-in `GammaJet` selection was used which applies a set of loose $\gamma + jet$ selection criteria and thereby reduces the size of the data sample to about 30%. The final analysis was performed on the produced root-tuples.

The criteria used in the `GammaJet` selection are listed below:

a. One of the triggers listed in Table 4.3 must be satisfied by the event.

b. There must be at least one electromagnetic object reconstructed, and the leading one must have transverse momentum 3 GeV above the L3 threshold of one of the fired triggers (see Section 4.3.2 and Table 4.3 for details). The leading EM must also fulfill the criteria listed in Table 4.2.

c. The most probable primary vertex found by the `d0root` algorithm must be within 60 cm of the centre of the detector, and there must be at least three tracks assigned to it (see Section 4.3.7).

isolation < 0.15
$f_{EM} > 0.9$
`hmx7` < 20
$\lvert\eta_\gamma\rvert < 1.1$ or $1.5 < \lvert\eta_\gamma\rvert < 2.5$
$\chi^2_{trk-prob} < 0.01$
in fiducial

Table 4.2: The selection criteria applied to the leading electromagnetic objects in the pre-selection These parameters are explained in Section 4.3.4.

4.3 Event Selection

After the pre-selection, several criteria were applied to further purify the data sample. These are described in detail below in the order in which they are applied. The cumulative efficiency of the selection criteria are given in Section 4.3.9.

4.3.1 Bad Run Removal

Events belonging to "bad runs" were removed. A list of bad runs was obtained from [22], where a run was declared bad if any of the following criteria were met:

- More than 10% of the events were declared "noisy" by the `cal_event_quality` software. Events were labelled noisy if they fulfill either of the "ring of fire", "coherent noise" or "missing crate" criteria.
- More than 24 cells had their mean energy out of limits.
- More than 8 towers gave no signal.

4.3.2 Trigger Selection

All events in the `JESB` skim have, by definition, fired at least one isolated photon trigger. To examine the turn-on bias for the triggers, $p_{T\gamma}$ spectra were plotted for all events firing each individual trigger, and a threshold was applied to compare to the selection in previous jet response analyses. Some of these photon p_T distributions are shown in Figure 4.1, and all turn-on thresholds are given in Table 4.3. In future analyses I plan to increase the thresholds to completely remove this bias.

Major changes were introduced with the v12 trigger list. About 80% of the data uses pre v12 triggers. The most important triggers for pre v12 data are `EM_HI_SH`, `EM_MX_SH` and for low E_T `CEM5` and `EM_LO_SH`. For v12 data we have `E1_SHT20`, `E1_SH30`, and `EM5` provide valuable low E_T data.

Isolated photon triggers with multi-tower requirements at L1 were not used. Such triggers might bias our sample since one (or more) of the towers might have been fired by the jet.

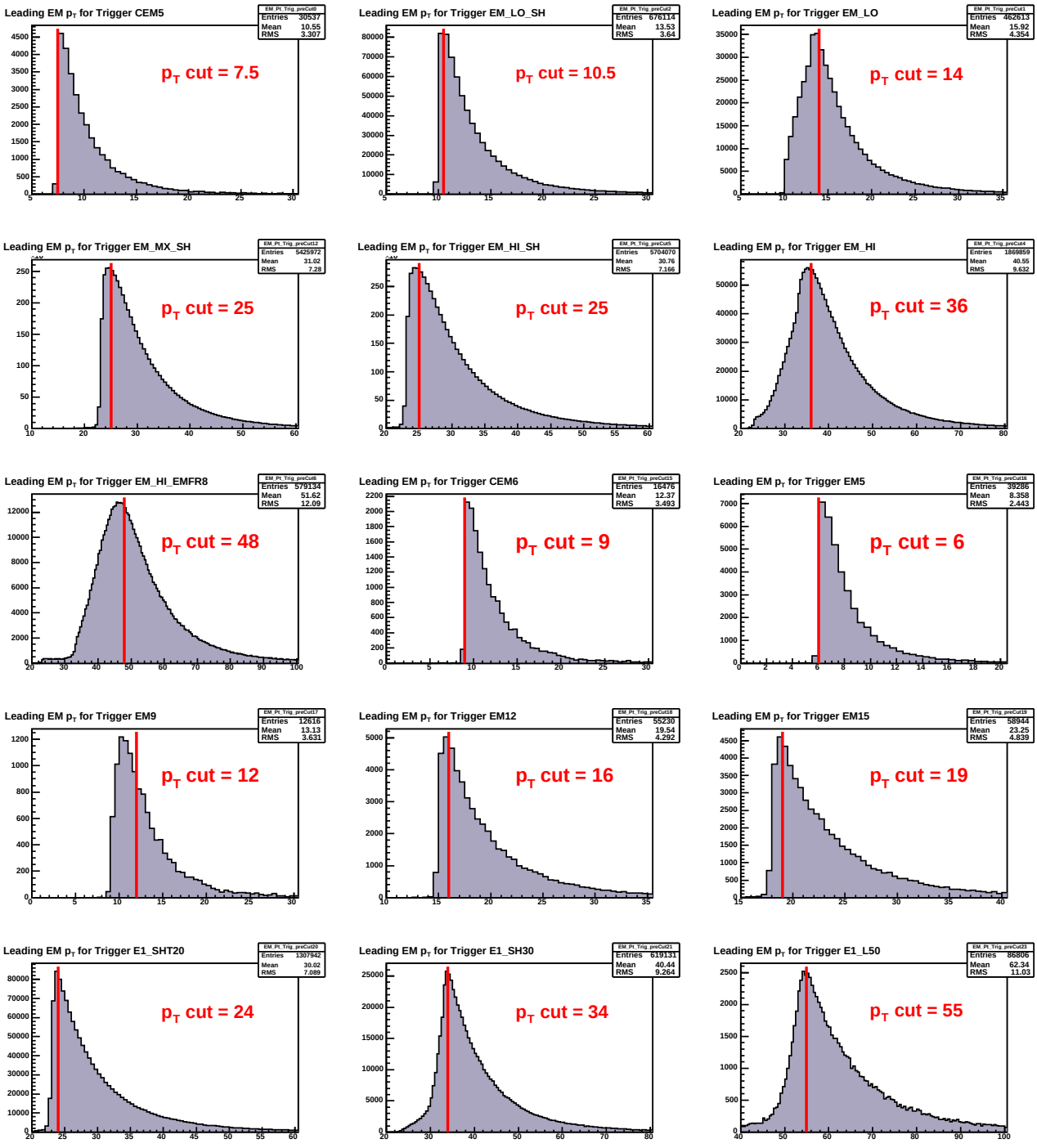

Figure 4.1: Transverse momentum distributions of the reconstructed electromagnetic object for the events that fired different direct photon triggers. The L3 threshold for each trigger is given in Table 4.3. The red line shows where the p_T selection was applied. All events with photon energy above this threshold are kept. Events with photon p_T below a certain trigger threshold might be kept, but only if they also fired another of the triggers and have p_T above the threshold of this trigger.

Trigger Name	L3 threshold	GammaJet	Our selection
CEM5	5	7.5	7.5
EM_LO_SH	7	10	10.5
EM_LO	10	13	14
EM_HI_SH12	12	15	16
EM_HI_L2_SH	12	15	16
EM_HI_SH	20	23	25
EM_HI	30	33	36
EM_HI_EMFR8	40	43	48
EM_HI_F0	50	53	57
EM_MX_SH	20	23	25
EM_MX	30	33	36
EM_MX_EMFR8	40	43	48
EM_MX_F0	50	53	58
CEM6	6	9	9
EM5	5	6	6
EM9	9	12	12
EM12	12	15	16
EM15	15	18	19
E1_SHT20	20	23	24
E1_SH30	30	33	34
E1_L50	50	53	55
E1_VL70	70	73	77

Table 4.3: The L3 EM p_T threshold, the GammaJet pre-selection and our final threshold for each isolated photon trigger. The first 13 are pre v12 triggers. The last nine are v12 triggers.

4.3.3 Jet Selection

Each event had to contain at least one Run II jet fulfilling the p14 criteria and not overlapping the EM object. The p14 criteria given in Table 4.4 include criteria on the electromagnetic fraction, coarse hadronic fraction and the hot fraction (the ratio between the highest and the next-to-highest p_T tower). The jet must also be L1 confirmed meaning that at least 40% (20% in the ICR) of the uncorrected jet energy must be measured in the L1 calorimeter towers within 0.5 ($\Delta R < 0.5$) of the jet centre.

In order to improve the response measurement at low energies, the jet p_T reconstruction threshold (Min_Jet_ET) was lowered to 3 GeV from the standard 8 GeV. This pushes the low E_T bias of the response measurement described in Section 3.8 to lower E_T. A detailed study of possible systematic effects of this lower threshold is given in Section 6.1.

Also, selection criteria on $\eta_{detector}$ of the leading jets were applied to ensure that most of the jet energy was deposited in the well measured parts of the detector, *i.e.* either in the central calorimeter or in one of the end caps. This selection is discussed separately in Section 4.3.8.

EM selection	Jet selection
$p_T > 6$ GeV	$0.05 < f_{EM} < 0.95$
$f_{EM} > 0.9$	$f_{CH} < 0.4$
`hmx7` < 12	$f_{hot} < 10$
isolation < 0.15	`n90` ≥ 2
$\lvert\eta_\gamma\rvert < 1.0$ or $1.6 < \lvert\eta_\gamma\rvert < 2.5$	L1 confirmed
$\chi^2_{trk-prob} < 0.01$	
in fiducial	

Table 4.4: The selection criteria for photons and the jets. Some of the EM criteria were applied already by the pre-selection as can be seen in Table 4.2.

4.3.4 Photon Selection

Each event was required to have exactly one electromagnetic object reconstructed fulfilling the quality criteria listed in Table 4.4. Most of these selections are the standard p14 criteria.

Only electromagnetic objects reconstructed with $p_T > 6$ GeV were saved by `top_analyze`, but after the trigger selection described in Section 4.3.2 no EM objects remain with $p_T < 7.5$ GeV.

To remove photon candidates that actually are jets, criteria were applied on the electromagnetic fraction, the isolation of the cluster and on the χ^2 of the H-matrix (`hmx7`). The H-matrix reflects the difference between the shape of EM shower in the calorimeter and what is expected from Monte Carlo. To ensure a well measured cluster, the photon candidate was required to be in-fiducial (*i.e.* not too close to cracks between towers) and either in the central calorimeter ($|\eta_{det}| < 1.0$) or in any of the end caps ($1.5 < |\eta_{det}| < 2.5$). Finally, if there was a track match it had to be very loose (probability less than 1%).

4.3.5 Bad Jet Removal

To remove noisy events from the sample, events with at least one "bad jet" above 8 GeV were removed. A bad jet is defined as a Run II jet not overlapping with an EM object

that does not fulfill all the p14 criteria. Before this selection 46% of our events had at least one "bad jet". About half of these events were removed when the selection criteria was applied.

4.3.6 Back-to-back Selection

Calculating the jet response using the Missing E_T Projection Fraction Method is based on a two body process where we have a jet back-to-back in the transverse plane with a photon. Events where this is not the case, for instance events where the hadronic recoil of the photon contains more than one jet due to gluon radiation, will generally give a lower response.

To make sure the photon and leading jet are back-to-back, a criterion is applied on the azimuthal angle between them. In jet response measurements during Run I, the selection $\Delta\phi > 2.8$ (160 degrees) was used. In previous studies, the shape of the response curves of the different cryostats only matched in the case of a tighter $\Delta\phi$ selection [5]. To be able to compare to these studies, the quite strict $\Delta\phi > 3.1$ (177.6 degrees) was used.

The systematic effect of varying this back-to-back selection is studied in Section 6.3.

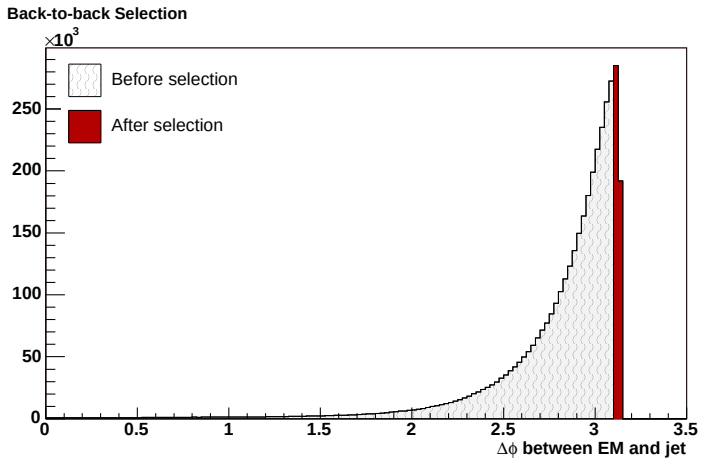

Figure 4.2: $\Delta\phi$ distribution, where $\Delta\phi$ is the azimuthal angle between the electromagnetic object and the leading jet. The low number of events in the bin close to π is due to a binning effect.

4.3.7 Vertex Criteria

A well determined primary vertex is important for correct object reconstruction and calculation of the $\not\!\!E_T$. Therefore, it was required that there was exactly one vertex found with at least three tracks. Furthermore, the z-coordinate of the vertex had to be within 50 cm of the centre of the calorimeter, since the tracking efficiency is better in the centre of the detector and since the calorimeter towers no longer are projective for large $|z_{vtx}|$.

`top_analyze Stradivarius` has access to two lists of primary vertices calculated by different vertex finding algorithms. The `d0reco` vertex, which is the one used during the object reconstruction, and the so-called `d0root` vertex, which uses a probabilistic method with some more constraints on the z-clustering, [23] are both available. The vertex selection described above was made on the `d0root` primary vertex, but since all objects are reconstructed with respect to the `d0reco` vertex it was required that the z-coordinates of the `d0root` primary vertex was within 2 cm of the reco primary vertex.

4.3.8 Cryostat Division

The jet response is not the same in the different cryostats. In Run I data, the jet responses in the end caps were very close to each other, but different from the response in the central calorimeter. In Run II, we observe quite different responses between the north and south end caps. Therefore the data are divided into three sub-samples depending on which cryostat the leading jet was measured in, and the response was measured separately in each sub sample.

To ensure that most of the jet cluster is well contained in the central calorimeter we apply a quite strict requirement on the detector η of the leading jet. The η_{det} is the η obtained from the centre of the detector (no jets are accepted close to the poorly instrumented ICR region ($0.7 < |\eta_{jet}| < 1.6$), and also events with very forward jets are removed.

$$\text{Central Calorimeter, CC} \qquad |\eta_{jet}| < 0.5 \tag{4.1}$$

$$\text{North End Calorimeter, NEC} \qquad -2.5 < \eta_{jet} < -1.8 \tag{4.2}$$

$$\text{South End Calorimeter, SEC} \qquad 1.8 < \eta_{jet} < 2.5 \tag{4.3}$$

As one can see there are many jets in the inter cryostat region (ICR). The jet response in the ICR is studied separately using either *di-jet* or $\gamma + jet$ events [24]. This is not done in this study.

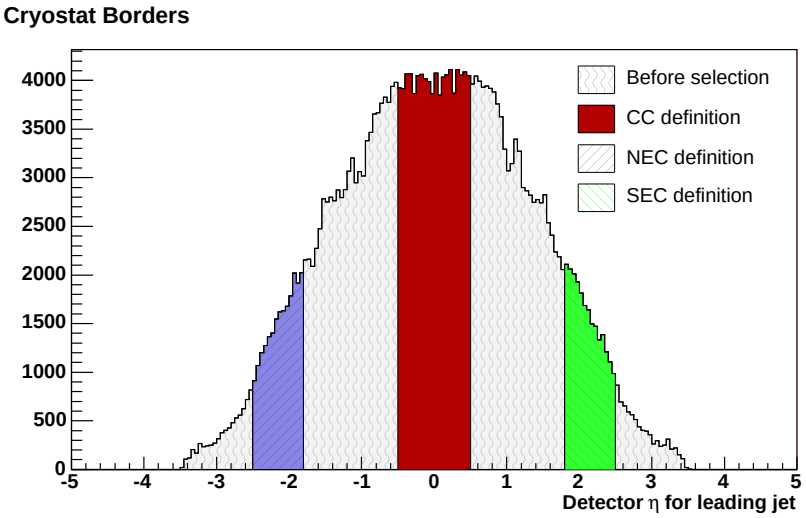

Figure 4.3: The η_{det} distribution of the leading jet. The coloured areas are kept, which correspond to just under half of the events.

4.3.9 Selection Summary

The efficiencies of the selection criteria are given in Table 4.5. It should be noted that these efficiencies are for the data that already passed the pre-selection described in Section 4.2. Earlier studies have also used criteria on the $\not\!\!E_T$ to remove $W + jet \rightarrow e + \nu + jet$ events. This selection was introduced during Run I when there was no magnetic tracking and is now not necessary. Less than 0.05% of the events would be removed by this selection, and these events look like a natural high end tail of the $\not\!\!E_T / p_{T\gamma}$ distribution.

Selection	Cumulative efficiency	Relative efficiency
Bad run removal	97.5%	97.5%
Trigger selection	80.4%	82.4%
Jet selection	78.1%	97.1%
Photon selection	53.1%	68.0%
Bad jet removal	41.3%	77.4%
Back-to-back selection	5.14%	12.5%
Vertex criteria	3.24%	63.0%
Cryostat selection	1.34%	41.2%

Table 4.5: The different parts of the event selection and their total efficiency.

Chapter 5

Jet Response Measurement

This chapter explains how the methods described in Chapter 3 were applied in order to measure the jet response in the isolated photon sample selected as described in Chapter 4.

5.1 Energy Dependence

As described in Sections 3.5 – 3.8, the energy dependence of the jet response can be measured with good accuracy by binning our final sample in E' and by mapping the jet response to the measured jet energy in each E'-bin. As described in 4.3.8, we do this separately for the CC and each EC. The data points are then fitted to the theoretical prediction of Equation 3.8.

The different steps of the analysis are described in greater detail below:

a. For each event, E' and R_{jet} are calculated according to Equations 3.26 and 3.21. The measured jet energy and the jet response of the event are saved in different distributions depending on the cryostat of the leading jet, and to which E'-bin the event belongs. The E' bin-edges are (in GeV):

`6,9,12,15,20,25,30,40,55,70,90,120,160,200,250,300,350,400,500`

b. For each E'-bin we expect the jet response to take a Gaussian distribution. A Gaussian is therefore fitted to the R_{jet} distribution. The fits are given in Figures 5.1, 5.3 and 5.5. In order to avoid bias from tails in the distributions, the fits are only performed over the range $\langle R_{jet} \rangle \pm 2RMS$, where $\langle R_{jet} \rangle$ is the arithmetic mean. The jet response of each E'-bin was defined by the Gaussian mean of the fit, and the error of the response by the uncertainty on this mean returned by the fitter.

c. The measured jet energy distributions for each E' bin in the different cryostats are shown in Figures 5.2, 5.4 and 5.6. The measured jet energies do not quite take Gaussian distributions. Just like has been the case in previous analyses [2, 3, 4, 5], E_{jet}^{meas} of a given E'-bin was defined the arithmetic mean.

The jet response is plotted against the mean E' value of each E' bin in Figure 5.7. Only E'-bins with at least 100 entries are shown. Clearly, there is a significant shift between the different cryostats. The response also seems to increase logarithmically with energy as expected by the Simple Jet Model described in Section 3.2.

The E_{jet}^{meas} is plotted against E' in Figure 5.8, *i.e* the measured energy versus the "true" energy. If E' would be a perfect estimator of the true jet energy, and if the jet algorithm and energy offset influences on the measured jet energy would be negligible, then we would expect the slope of E_{jet}^{meas} versus E' to be the response (see Equation 3.13 with $R_{cone} = 1$ and $E_O = 0$ GeV). We see a nearly linear relationship.

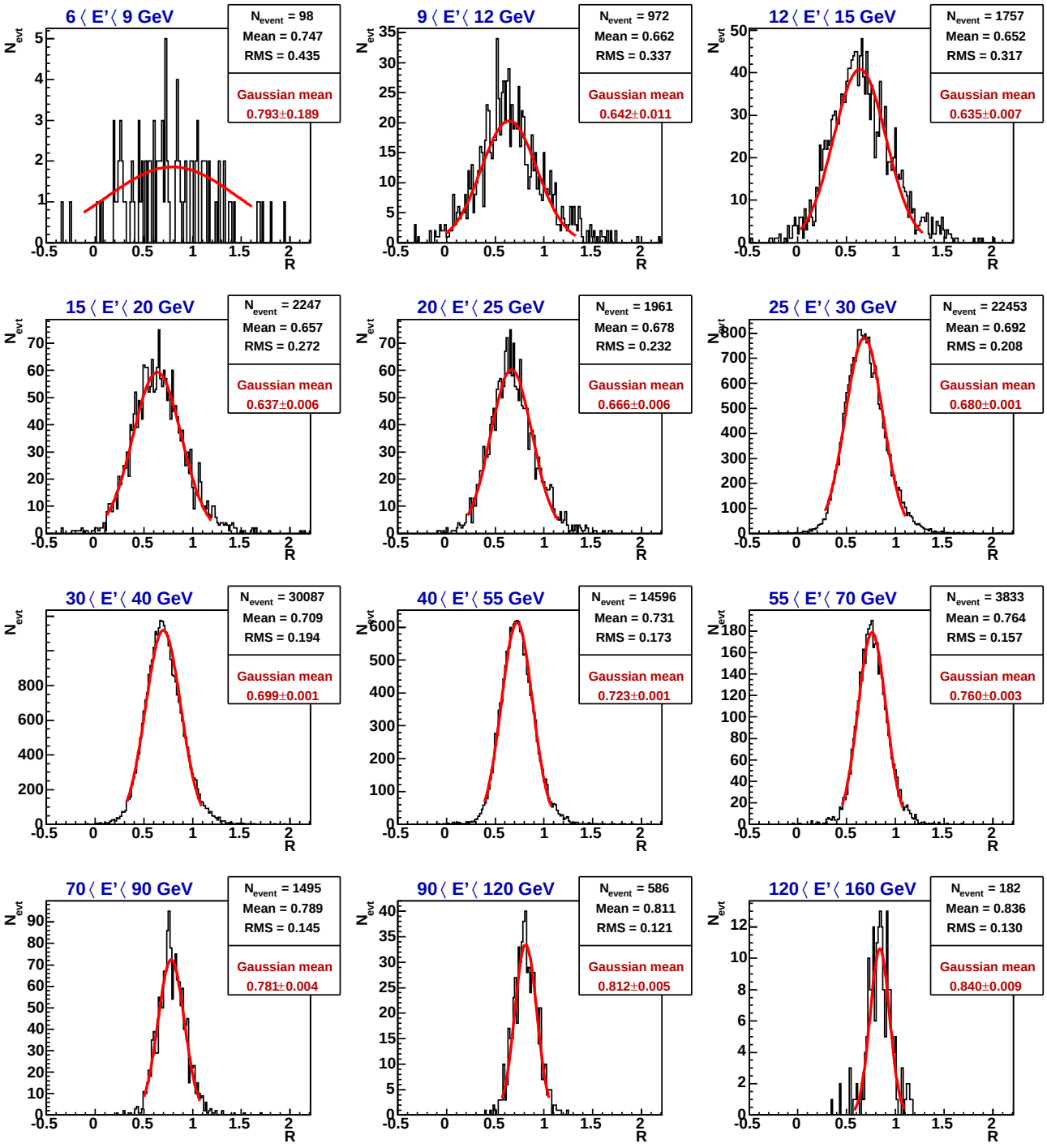

Figure 5.1: Jet response distributions in different E' bins for jets in the Central Calorimeter.

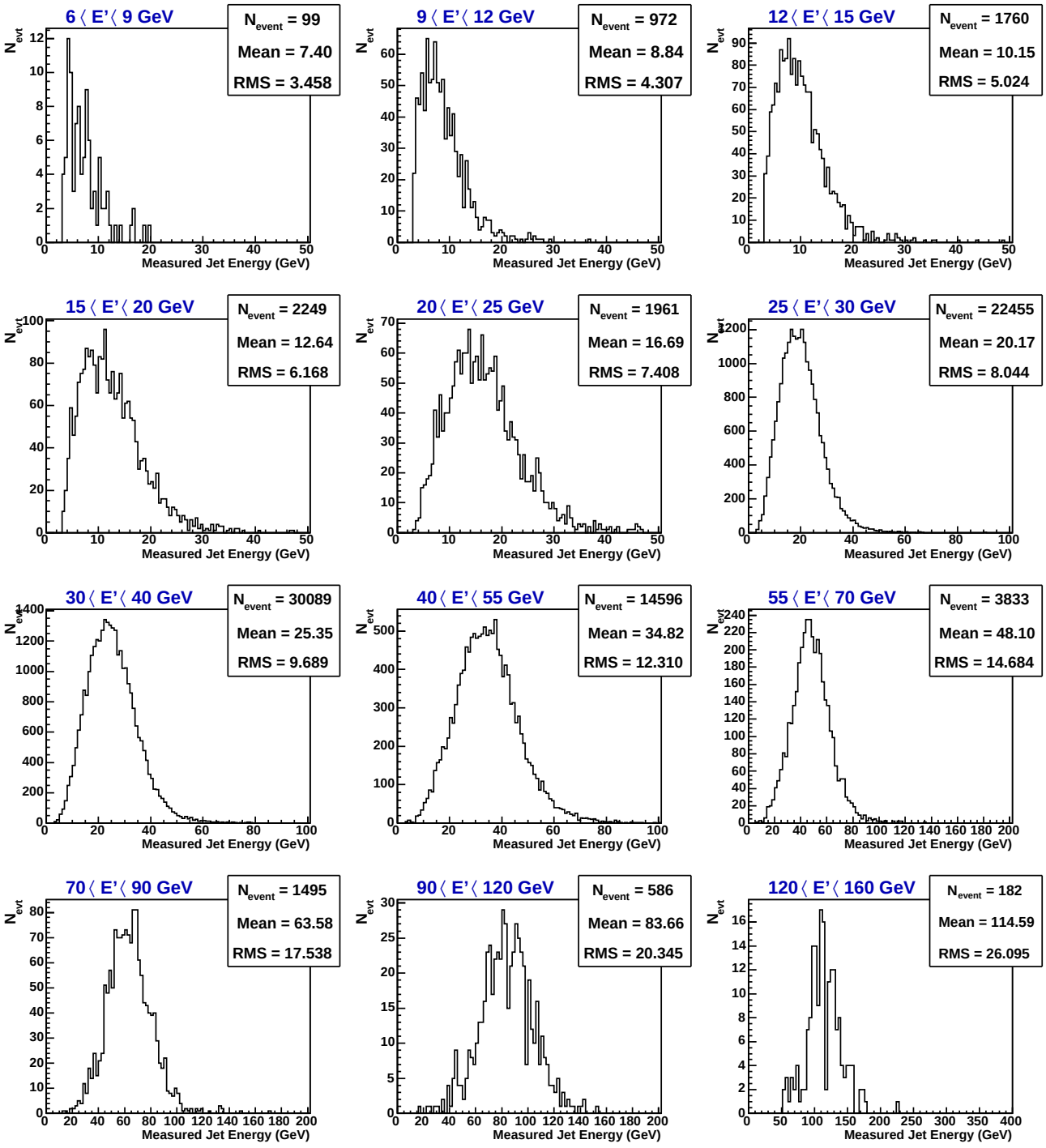

Figure 5.2: Measured jet energy distributions in different E' bins for jets in the Central Calorimeter.

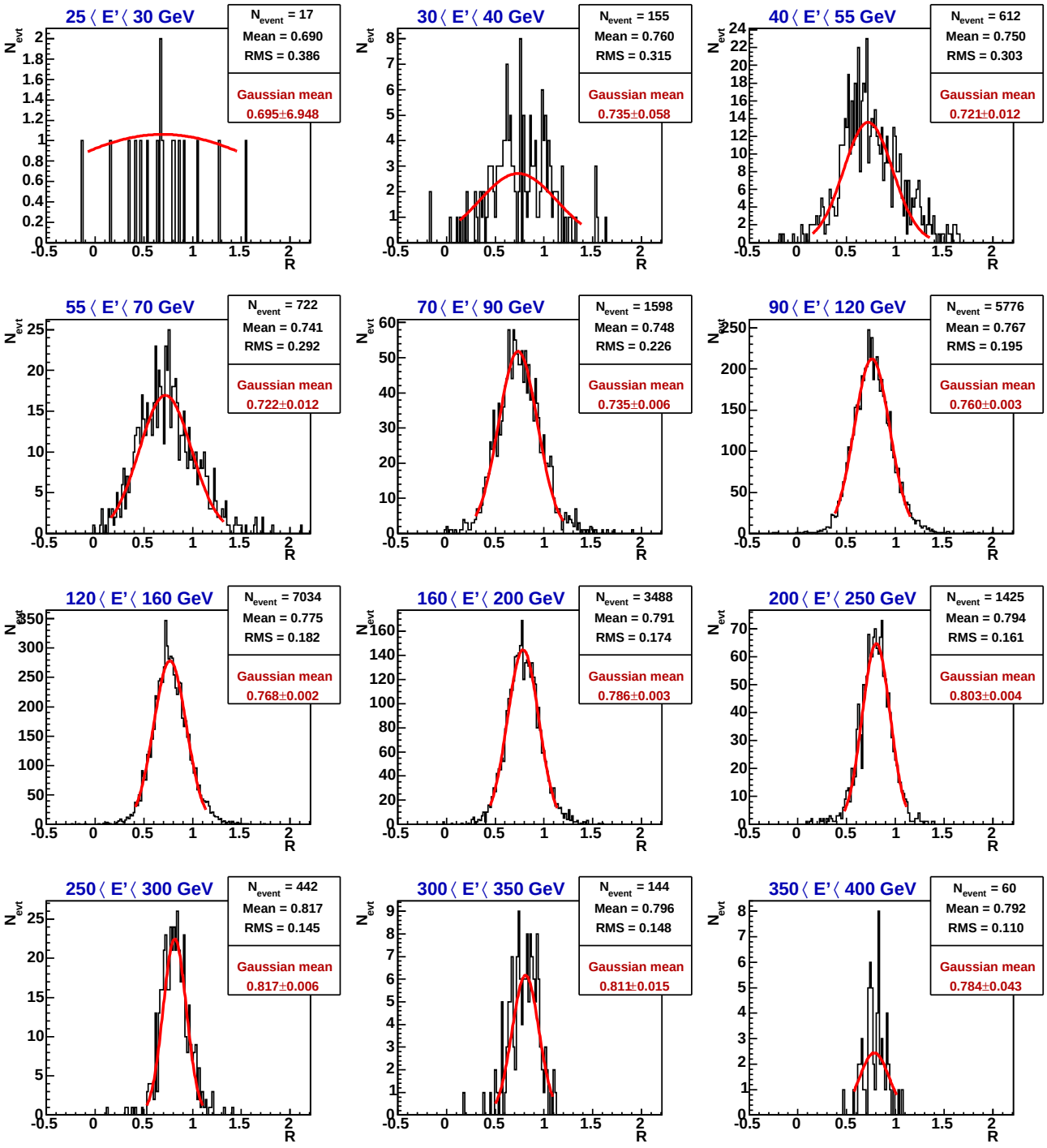

Figure 5.3: Jet response distributions in different E' bins for jets in the North Calorimeter.

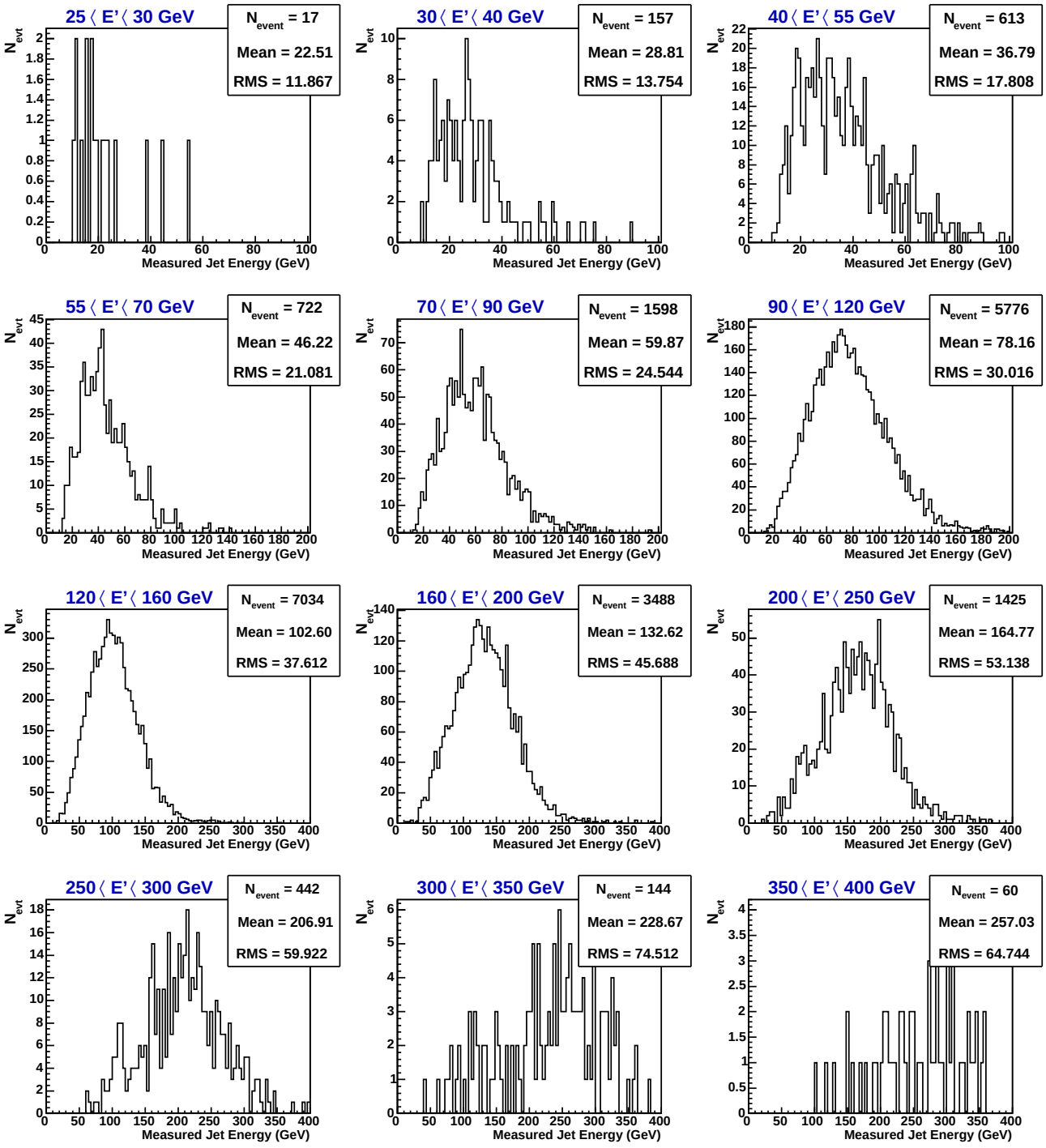

Figure 5.4: Measured jet energy distributions in different E' bins for jets in the North Calorimeter.

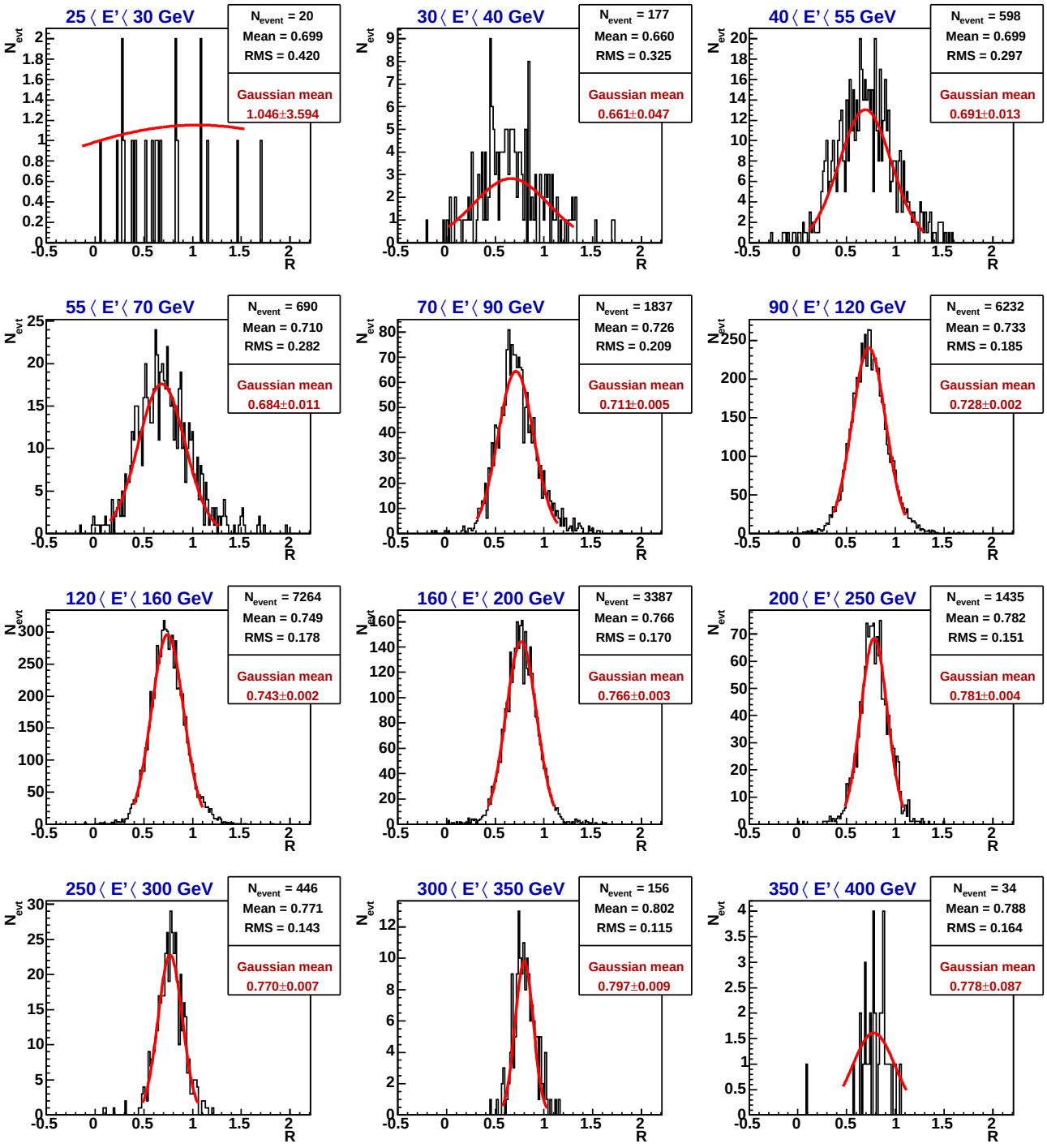

Figure 5.5: Jet response distributions in different E' bins for jets in the South Calorimeter.

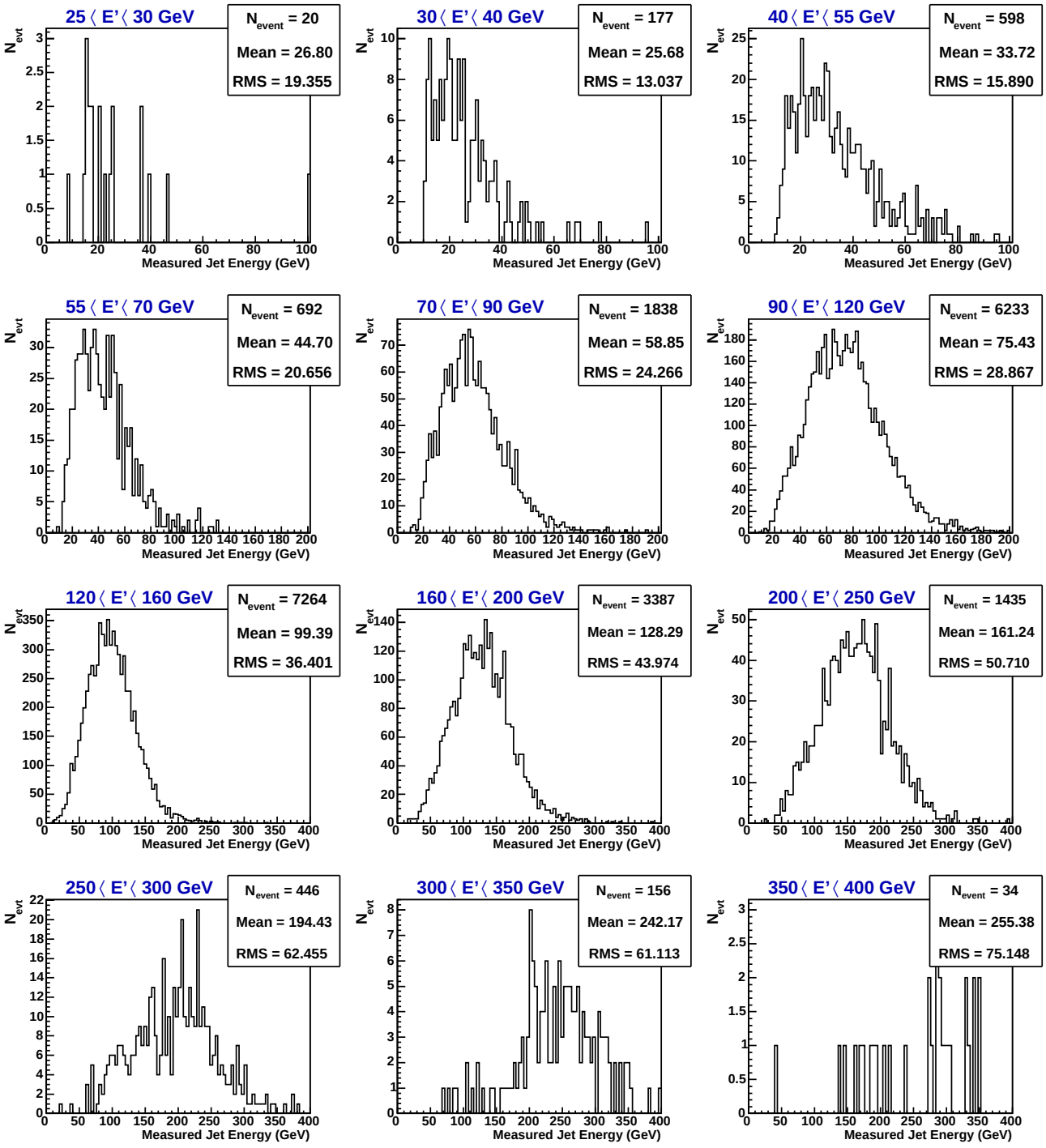

Figure 5.6: Measured jet energy distributions in different E' bins for jets in the South Calorimeter.

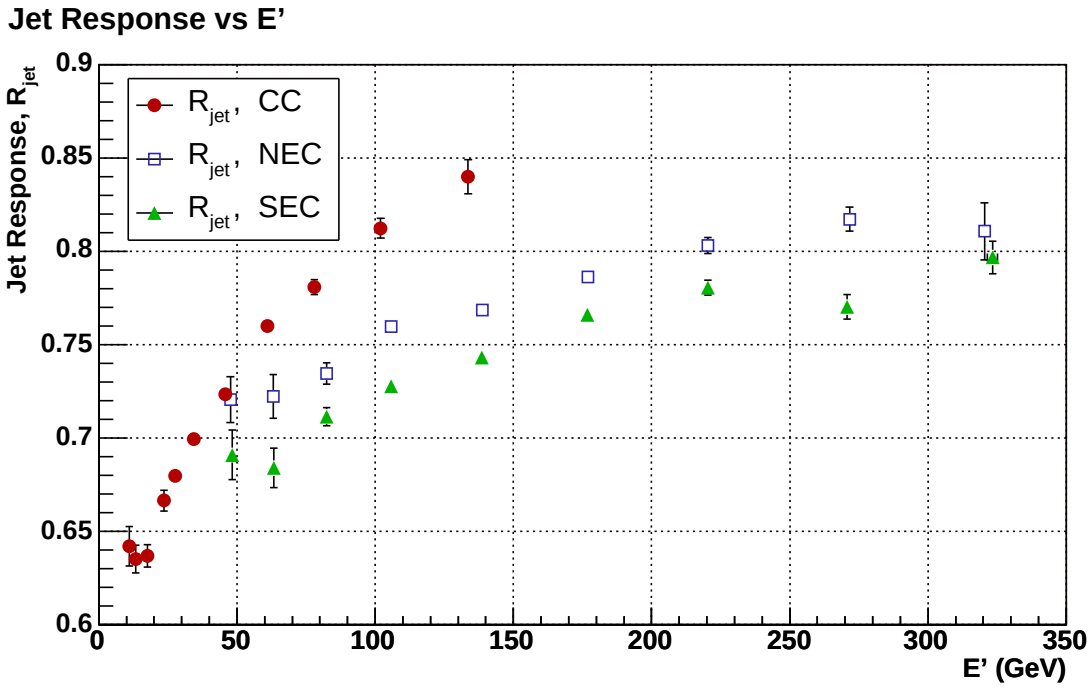

Figure 5.7: Jet response vs E'. The response values are the Gaussian means of the fits seen in Figures 5.1, 5.3 and 5.5. The E' value of a given point is the arithmetical mean for the events within the bin. Only E'-bins containing at least 100 events are shown.

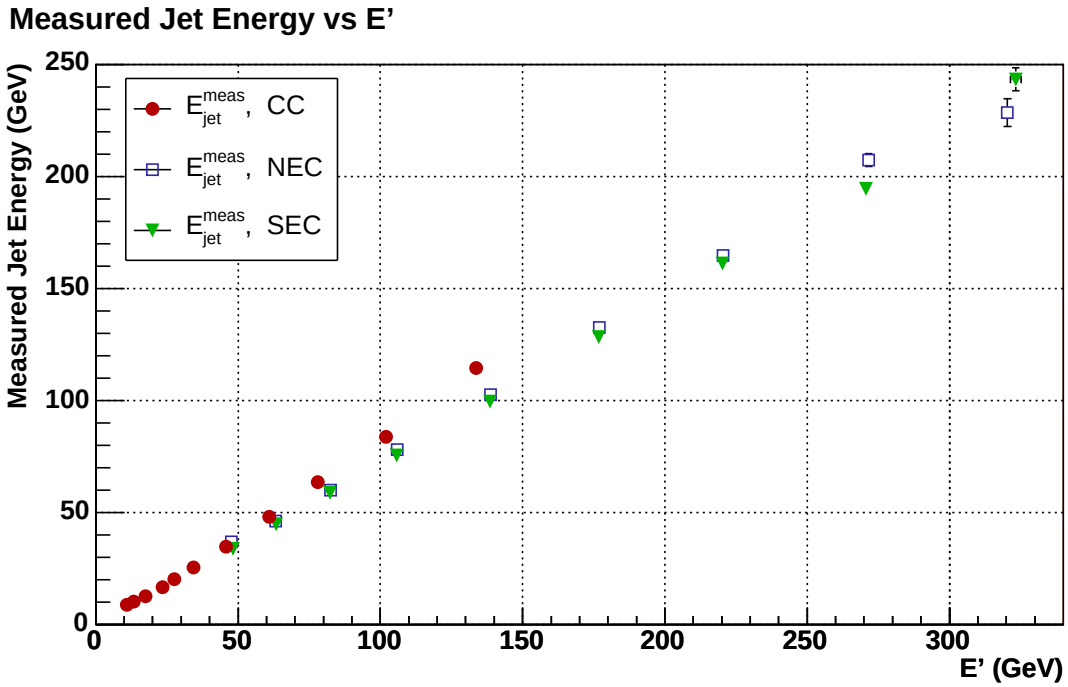

Figure 5.8: Measured jet energy vs E'. Only E'-bins containing at least 100 events are shown.

5.2 Cryostat Correction

Different calorimeter crates are known to give different responses to electromagnetic objects from the EM scale studies. We therefore expect to also see a different jet response in the each cryostat. Since the cryostats were built using the same technology, it is reasonable to assume that their jet responses have the same energy dependence, but only need to be scaled by a constant factor to match. The EM scale difference between crates is typically 1 or 2%. For jets we see a 8% difference between the central and the south cryostats. The magnitude of this difference not fully understood.

To take the shift between the cryostats into account we have introduced two cryostat factors defined as:

$$F_{\rm cryo}^{\rm NEC} = \frac{R_{jet}^{\rm NEC}}{R_{jet}^{\rm CC}} \quad \text{and} \quad F_{\rm cryo}^{\rm SEC} = \frac{R_{jet}^{\rm SEC}}{R_{jet}^{\rm CC}}. \tag{5.1}$$

5.3 Fitting Procedure

The final plot of R_{jet} versus E_{jet}^{meas} for each of the three cryostats can be obtained through mapping the response of Figure 5.7 on to E_{jet}^{meas} by using Figure 5.8. As discussed in the previous section, we expect the response in each cryostat to have the same energy dependence. It should only need to be scaled by a constant cryostat factor. In Sections 3.1 and 3.2 we derived the expected energy dependence to follow Equation 3.8. This gives us five parameters to obtain from fits of the three cryostat datasets; an offset, logarithmic slope and a curvature (parameters p_0 – p_2 of Equation 3.8) and the two cryostat factors.

The fit is accomplished by minimizing the following function:

$$\begin{aligned}
\chi^2 \;=\; & \sum_{i\in \rm CC} \left(\frac{\langle R_{jet}\rangle_i - (p_0 + p_1 \ln(\langle E_{jet}^{meas}\rangle_i/E_0) + p_2 \ln^2(\langle E_{jet}^{meas}\rangle_i/E_0))}{\sigma_i} \right)^2 + \\
& \sum_{i\in \rm NEC} \left(\frac{\langle R_{jet}\rangle_i - F_{\rm cryo}^{\rm NEC}(p_0 + p_1 \ln(\langle E_{jet}^{meas}\rangle_i/E_0) + p_2 \ln^2(\langle E_{jet}^{meas}\rangle_i/E_0))}{\sigma_i} \right)^2 + \\
& \sum_{i\in \rm SEC} \left(\frac{\langle R_{jet}\rangle_i - F_{\rm cryo}^{\rm SEC}(p_0 + p_1 \ln(\langle E_{jet}^{meas}\rangle_i/E_0) + p_2 \ln^2(\langle E_{jet}^{meas}\rangle_i/E_0))}{\sigma_i} \right)^2
\end{aligned} \tag{5.2}$$

Here, $\langle R_{jet}\rangle_i$ is the Gaussian mean from the fit to the response distribution in E'-bin i, $\langle E_{jet}^{meas}\rangle_i$ is the mean measured jet energy in the same bin, and E_0 is an energy constant.

This constant was set to 100 GeV, which is a typical value of $\langle E_{jet}^{meas} \rangle$, in order to reduce the correlations between the parameters of the fit [5].

In order to ensure a reasonable quality on $\langle R_{jet} \rangle_i$, only E'-bins with at least 100 entries were used for the fit. Also the data points clearly influenced by the low E_T bias were not included in the fit.

5.3.1 Result

The final plots of the measured jet response versus the measured jet energy in the different cryostats are shown together with the global fit in Figure 5.9.

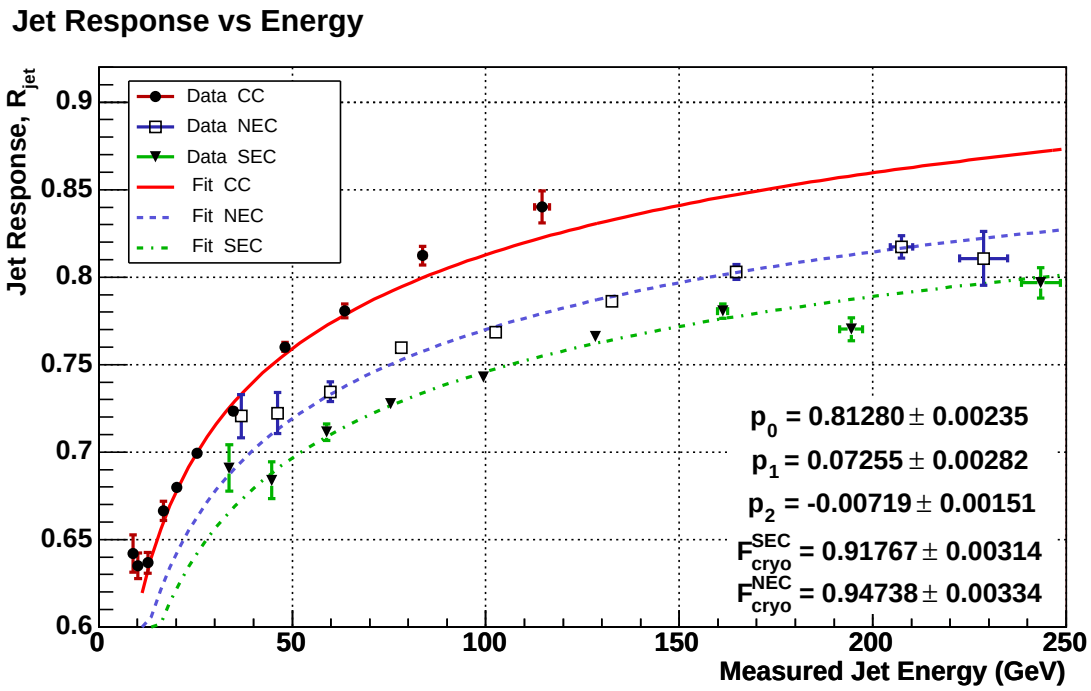

Figure 5.9: The final jet response measurement in the three cryostat regions vs the measured jet energy. All data points shown were used for the fit except the first two in the Central Calorimeter and the first point of each End Cap. These points were excluded since they are biased by the jet reconstruction threshold as described in Section 3.8.

The jet response in the DØ calorimeters is parameterized according to Equation 3.8 on the form

$$R_{jet} = F_{\text{cryo}} \left(p_0 + p_1 \ln \frac{E_{jet}^{meas}}{E_0} + p_2 \ln^2 \frac{E_{jet}^{meas}}{E_0} \right),$$

where $E_0 = 100$ GeV and $F_{\text{cryo}} = 1$ in the CC by definition. The other parameters and their uncertainties given from the fit (described in Section 5.3) are:

$$\begin{aligned} p_0 &= 0.8128 \pm 0.0024 \\ p_1 &= 0.0725 \pm 0.0028 \\ p_2 &= -0.0072 \pm 0.0015 \\ F_{\text{cryo}}^{\text{NEC}} &= 0.9474 \pm 0.0033 \\ F_{\text{cryo}}^{\text{SEC}} &= 0.9177 \pm 0.0031 \end{aligned} \tag{5.3}$$

5.3.2 Result Comparison

In Figures 5.10 and 5.11, our measurement is compared to data from the `jetcorr 5.3` analysis [5], the most recent official response measurement. `jetcorr 5.3` used the standard 8 GeV jet p_T jet reconstruction threshold and hence suffers more from the low E_T bias. In the CC, no data points with E_{jet}^{meas} below 20 GeV were used for the `jetcorr 5.3` fit, and in the ECs events were required to have $p_{T\gamma} > 25$ GeV and $E' > 100$ GeV. The reason for the strict criteria in the ECs is that the low E_T bias here is present at much higher energies since jet reconstruction threshold is given in jet p_T. $E_T = 20$ GeV at $\eta = 0$ corresponds to the energy 20 GeV, but $E_T = 20$ GeV at $\eta = \pm 2.15$ (in the middle of the End Caps) corresponds to $E = E_T \cosh 2.15 \approx 87$ GeV.

In the central calorimeter, our data points appear to be free of low E_T bias down to 12 GeV. The low E_T bias seems to impact `jetcorr` results up to 20 GeV.

The improvement is even more noticeable in the forward cryostats as can be seen in Figure 5.11. The low E_T reach in previous analyses have been down to 80-100 GeV. We are now using points down to 45 GeV.

It should be pointed out that our measurement agrees very well with `jetcorr 5.3` at energies above the low E_T bias. This implies that there are no significant systematic effects introduced when lowering the jet reconstruction threshold. This will further be discussed in Section 6.1.

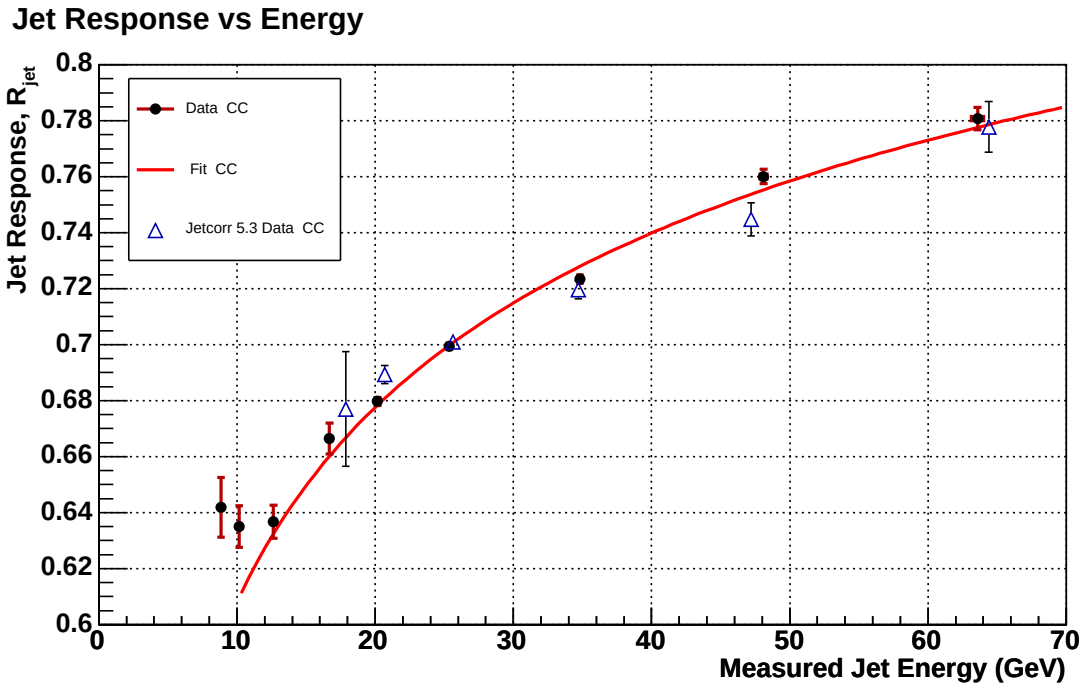

Figure 5.10: Comparison of our results in the CC with the jetcorr 5.3 measurement which used an 8 GeV jet clustering cut. The curve is the fit of our data with fit parameters given in Section 5.3.1.

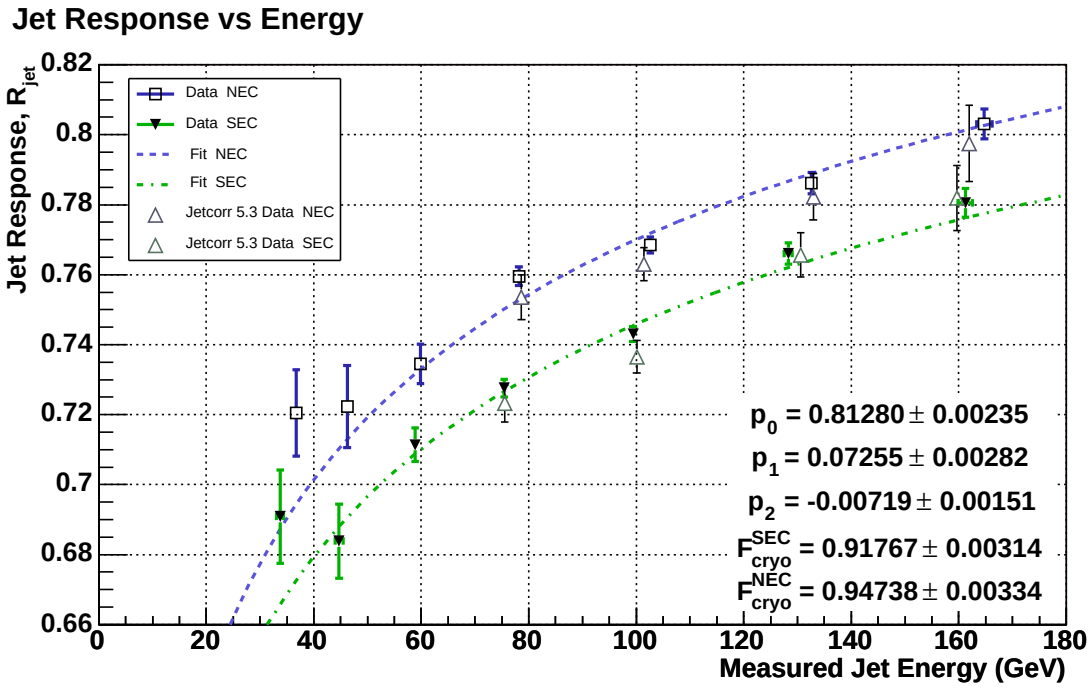

Figure 5.11: Comparison of our jet response in the North and South cryostats with an earlier measurement that is using the 8 GeV jet clustering cut. The curve is the fit of our data with fit parameters given in Section 5.3.1.

5.3.3 Low E_T Improvements

In order to study the improvement of the R_{jet} measurement at low E_T due to the lowered jet reconstruction threshold, but also to examine possible systematic biases, part of our input data sample ($\approx 7\%$) was processed also with the standard 8 GeV jet reconstruction threshold. This data was compared with the exact same events from our original data sample using the 3 GeV jet threshold. A study of how the reconstructed jets were affected by the different thresholds is given in Section 6.1.

All selection criteria given in Chapter 4 were applied to the two samples, and the jet response was measured much in the same way as described in Section 5.1, but due to the limited statistics, E'-bins with width 10 GeV were used.

The result, R_{jet} vs E_{jet}^{meas}, in the CC is shown in Figure 5.12. We can see that the low E_T bias seems to take on at jet energies between 20-25 GeV using the 8 GeV threshold and that the reach at low jet energies is extended using the 3 GeV jet threshold.

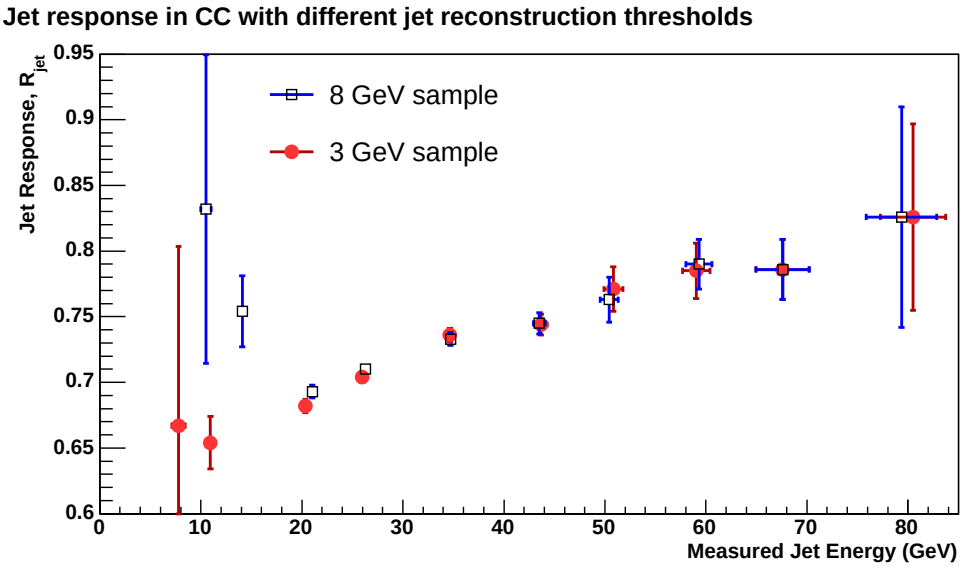

Figure 5.12: Jet response versus measured jet energy in two samples using different jet p_T reconstruction thresholds. The low E_T bias is visible at energies below 25 GeV. Using a lower jet reconstruction threshold improves the measurement in this region.

The results agree well with the expectations given in Section 3.8. We expected response measurements to be weakly biased in E' bins where the mean measured jet E_T was about 20 GeV when using the standard 8 GeV clustering cut. In E'-bin 20-30 GeV, the mean

measured jet energy (which is close to E_T^{meas} since we are in the CC) is about 21 GeV. Here, the response measures 1.6% higher using the 8 GeV clustering cut. In the E'-bin 10-20 GeV, the difference is 15%.

In Figure 5.13, the R_{jet}-distributions for these two E'-bins are shown. In the 3 GeV sample we see new events with low p_T jets. These events have a low response, and appear in the low region of each response distributions.

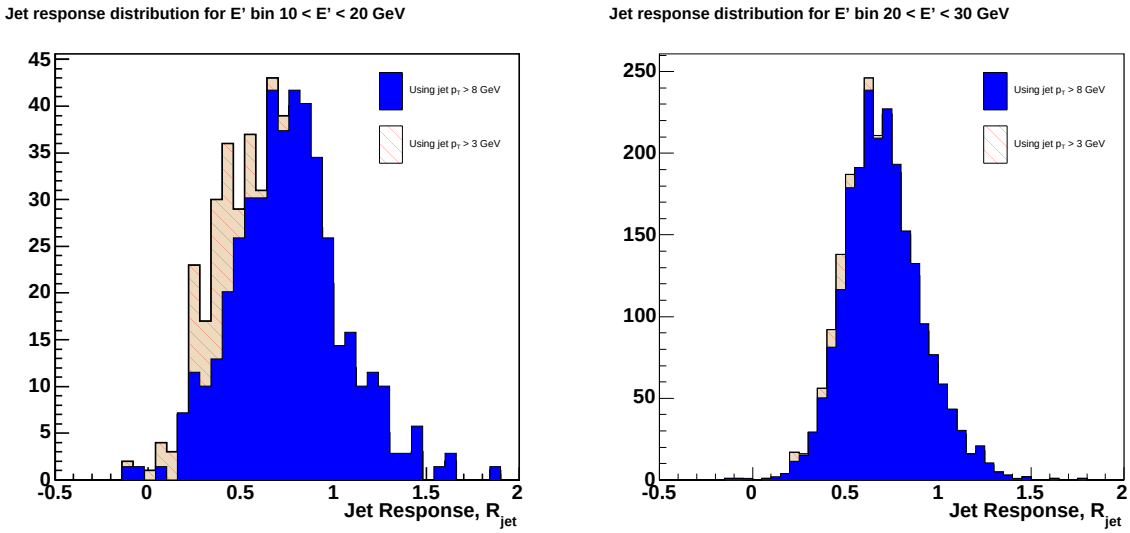

Figure 5.13: Jet response distributions for two E'-bins for two different data samples using different jet reconstruction thresholds. The samples contain the exact same events before the events selection. New low E_T jets with low response appear in the sample using the lower jet threshold. The left distributions correspond to the points with measured jet energy at $\approx$ 11 GeV (3 GeV sample) and at $\approx$ 14 GeV (8 GeV sample) in Figure 5.12. The right distributions correspond to the two points with measured jet energies at $\approx$ 21 GeV.

Chapter 6

Systematic Error Estimation

The systematic uncertainties we here consider are: possible jet threshold effects, quality criteria on the photon, and the criterion of how back-to-back the jet and photon really are.

6.1 Jet Threshold Systematics

Lowering the jet p_T threshold results in new low energy jets being found, not only since final jets with lower p_T will be saved, but also since more iterations are allowed due to the 0.5×`Min_Jet_ET` termination (described in Step 3 of Section 3.3). When using the standard 8 GeV threshold, this means that only seeds with p_T greater than 4 GeV will be considered by the jet algorithm, and (after merging and splitting) only final jets with p_T greater than 8 GeV will be stored.

With the 3 GeV jet threshold used in this study, seeds with p_T as low as 1.5 GeV will be used by the jet finding algorithm. This will result in many new low p_T jets found, some of which will overlap with higher p_T jets resulting in new merges and splits.

In order to study how different jet thresholds affect the reconstructed jets, a subset (7%) of our data sample was re-processed with the standard 8 GeV jet p_T reconstruction threshold. This "8 GeV sample" was compared with the exact same events from our standard sample using the 3 GeV threshold (which will be referred to as the "3 GeV sample"). A comparison of the response measured in these samples is given in Section 5.3.3.

To study how the different jet thresholds affect the reconstructed jets, the jets in 150,000 specific events were compared event-by-event in the two samples. A few examples of the

number of reconstructed jets and their transverse momenta are given below:

a. 8 GeV sample: 1 jets with pT: 17.4789
3 GeV sample: 1 jets with pT: 17.4789

8 GeV sample: 0 jets with pT:
3 GeV sample: 5 jets with pT: 7.42461, 5.23312, 5.20587, 4.51049, 4.321

8 GeV sample: 3 jets with pT: 70.8362, 29.9873, 8.32918
3 GeV sample: 5 jets with pT: 70.8362, 29.9873, 8.32918, 7.38507, 3.4039

b. 8 GeV sample: 3 jets with pT: 14.7827, 10.0392, 8.1198
3 GeV sample: 5 jets with pT: 14.7827, 10.0392, 8.33797, 8.1198, 6.20294

c. 8 GeV sample: 1 jets with pT: 8.72348
3 GeV sample: 2 jets with pT: 10.7203, 8.72348

d. 8 GeV sample: 1 jets with pT: 12.8053
3 GeV sample: 3 jets with pT: 12.6655, 5.58035, 3.65001

The jets in the 8 GeV sample were categorised as:

- "identical" if they had a counterpart in the 3 GeV sample with $\Delta R < 0.001$ and $\Delta E < 0.001$ GeV
- "close" if there was a jet in the 3 GeV sample with $\Delta R < 0.2$
- "not identified" otherwise

The number of jets in the different categories are given against jet p_T in Figure 6.1.a. 91% of the jets in the 8 GeV sample had "identical" counterparts in the 3 GeV sample. These jets should all be defined by the exact same list of towers due to the strict definition of "identical" matches. Almost all the remaining jets had a "close" match, indicating that the jets are defined by the same energy cluster, but not exactly the same towers. Very few jets (0.45%) were "not identified" in the 3 GeV sample, and there are no such jets with p_T above 15 GeV.

In Figure 6.1.b, the same distributions are given, but only for leading jets. Here we have a new category, "no longer leading", for leading jets in the 8 GeV sample with an

"identical" or "close" match in the 3 GeV sample that is not the leading jet. An example of such a case is given in example **c.** above.

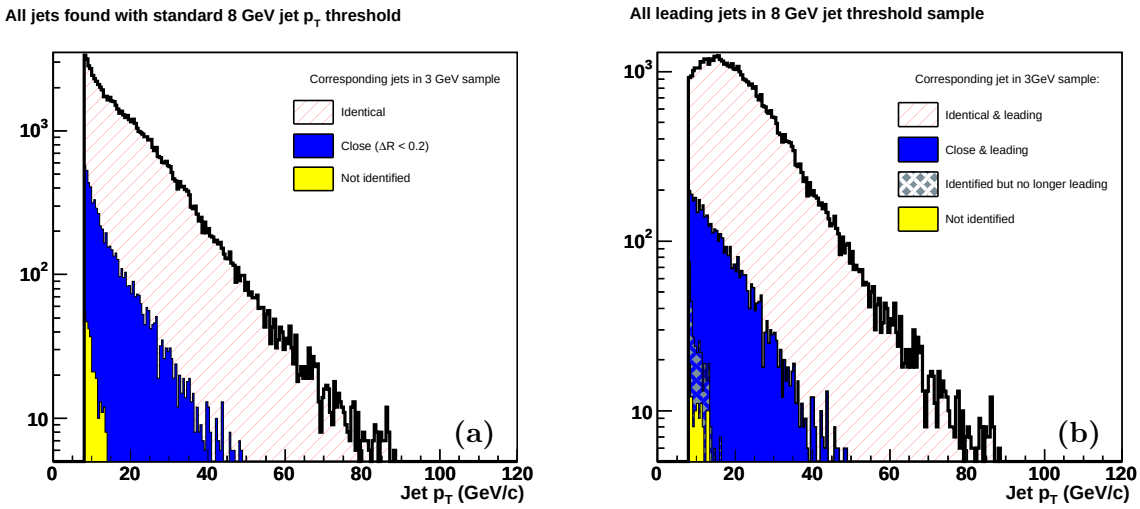

Figure 6.1: **a.** (left) Transverse momentum distributions of all jets in the 8 GeV sample. Jets are also classified as "identical" (hatched), "close" (blue) or "not identified" (yellow). **b.** (right) Transverse momentum distribution of the leading jets in the 8 GeV sample.

All 3 GeV sample jets were classified in the same manner with respect to the jets in the 8 GeV sample, but here with the category "new" instead of "not identified." 58% of all jets are in this category. Most (98.3%) of these are however below 8 GeV. The fraction of "new" jets for all jets above 8 GeV is 2.3%. p_T distributions for jets in the different categories are shown in Figure 6.2.a.

In Figure 6.2.b we see the same distributions for leading jets. For the leading jets above 8 GeV, 91.3% are identical and 7.6% are close. We have hereby seen that basically all of the jets in the sample with p_T above 15 GeV are either reconstructed "identical" or "close" with the different jet thresholds. We do expect new jets to be found in the 3 GeV sample up to about 15 GeV due to jet reconstruction inefficiencies in the 8 GeV sample. It would, however, not be good if we would also see differences in the reconstructed jets at higher energies since we want our measurement to be applicable for studies using the standard 8 GeV threshold. The "close" jets were therefore further examined.

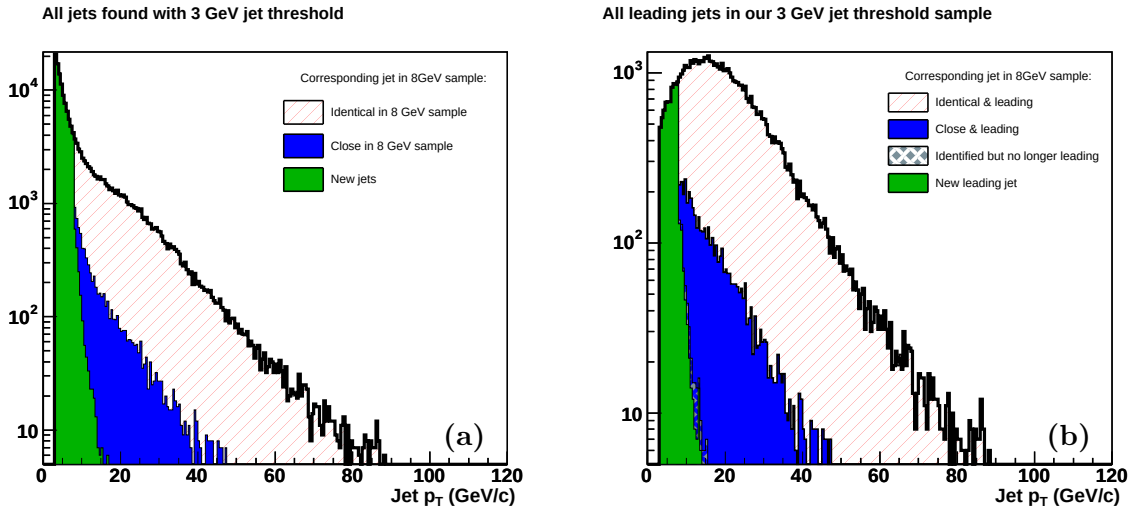

Figure 6.2: **a.** (left) Transverse momentum distribution of all jets in the 3 GeV sample. The jets are divided in three categories depending on whether there is a matching jet in the 8 GeV sample. **b.** (right) Transverse momentum distribution of the leading jets in the 3 GeV sample.

In Figure 6.3.a, the angular distance between the close jets are plotted. It can be seen that most of the matches are very close in space, especially for jets with energies above 15 GeV. In Figure 6.3.b we can see that most "close" jets also are reconstructed with very similar p_T in the two samples. Most matches have a p_T difference less than 1 GeV/c, but jets in the 8 GeV sample tend to have a somewhat higher energy.

Most of the jets reconstructed in the two samples had not experienced any merges or splits. Amongst the "close" jets, splits and merges where much more frequent, especially in the 3 GeV sample. In Figure 6.4.a the difference in the number of merges for each matching jet is plotted against the measured jet p_T. The majority of the "close" jets experience the same number of merges with the two reconstruction thresholds. It is slightly more frequent with merges for low p_T jets in the 3 GeV sample.

In Figure 6.4.b, the difference in number of split between "close" jets in the samples are shown. Here we see the reason for the asymmetry in Figure 6.3.b: most "close" jets have undergone an extra split in the 3 GeV sample and hence lost some energy (on average 0.2 GeV). The new low p_T jets found in the 3 GeV sample sometimes overlap partially with higher p_T jets and "steal" a low energy tower. This will cause some jets to

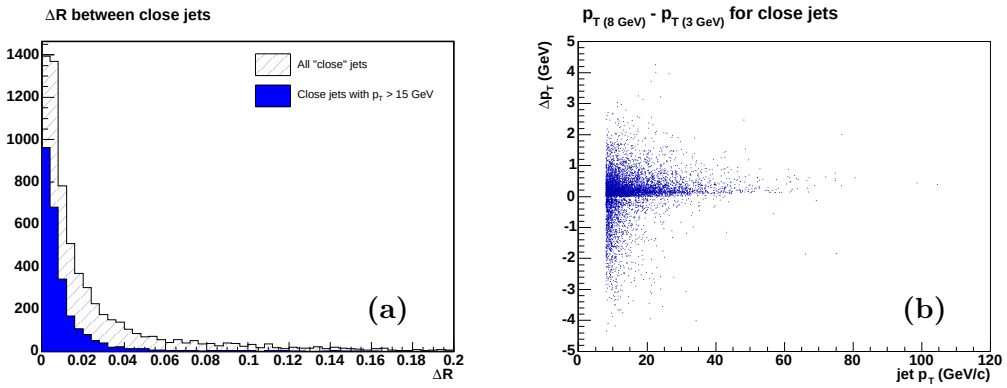

Figure 6.3: **a.** (left) Most of the "close" jets, defined as $\Delta R < 0.2$, are actually much closer in space. **b.** (right) The difference in transverse momenta between the "close" jets is also quite small, and becomes smaller with increasing p_T. There is an asymmetry in the Δp_T distribution, jets from the 8 GeV sample tend to have higher p_T.

be reconstructed with slightly lower energy and changed direction in the 3 GeV sample, which probably is the major occurrence that causes a non-perfect, *i.e.* only "close", match.

A new category "very close" was defined for matches with $\Delta R < 0.05$ and $\Delta p_T < 1$ GeV. The fraction of the jets in the 3 GeV sample with "very close" matches in the 8 GeV sample is given in Table 6.1. We can see that 99% of all jets above 12 GeV are in this category, and the fraction increases with jet p_T. We can hereby conclude that the Run II Cone Algorithm performs very similarly for jets with measured jet p_T above 12 GeV after lowering the jet p_T reconstruction threshold from 8 GeV to 3 GeV.

measured jet $p_T >$	8 GeV	12 GeV	16 GeV	20 GeV	30 GeV
identically reconstructed	89.39%	92.91%	94.16%	94.93%	95.99%
$\Delta R < 0.05$ and $\Delta p_T < 1$ GeV	96.55%	99.04%	99.37%	99.50%	99.75%

Table 6.1: Fraction of jets reconstructed with the 3 GeV threshold that are reconstructed identically or at least "very closely" ($\Delta R < 0.05$ and $\Delta p_T < 1$ GeV) using the standard 8 GeV sample.

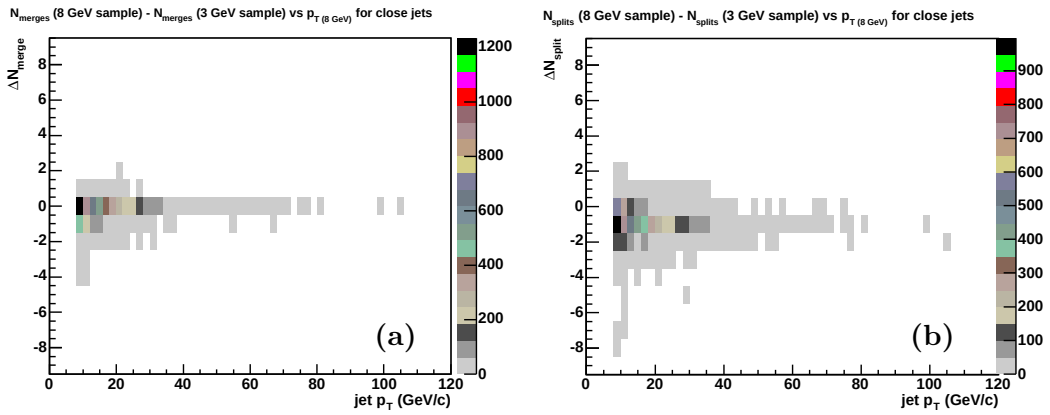

Figure 6.4: **a.** (left) Most of the "close" jets do experience the same number of merges with the different jet reconstruction thresholds. **b.** (right) Most of the "close" jets undergo one extra split using the lower jet threshold. This explains the asymmetry seen in Figure 6.3.b.

6.2 Photon Selection Systematics

H-Matrix 7 Systematics

The dominant part of the background in our sample comes from di-jet events. A jet that at an early stage produces energetic π_0's will deposit much of its energy in the EM part of the calorimeter and might be reconstructed as an electromagnetic object. Such mis-identified EM objects might qualify as an isolated photon through passing our EM selection criteria described in Section 4.3.4. In order to study the bias from such events the response was re-derived with different photon identification criteria.

The most efficient photon identification parameter listed in Table 4.4 is the χ^2 of the H-matrix, which reflects the difference between the shape of the EM shower in the calorimeter and what is expected in advanced simulations. Previous studies have used the criterion `hmx8` < 20. In this study the `hmx7` was used since the `hmx8` parameter is not available in `top_analyze Stradivarius`. The standard selection was `hmx7` < 12, which roughly corresponds to `hmx8` < 20.

The energy of jets reconstructed as photons has been EM scale corrected. The magnitude of a typical EM scale correction is an energy increase by 4% ($R_{em} \approx 0.96$). Since jets reconstructed as EM objects have a large electromagnetic fraction, we expect them to have a higher response than an average jet, but lower than the response of a true photon. The energy of a mis-identified photon after EM correction will hence (on average) be less than its true energy. When the "photon" energy is underestimated, the jet response will be measured too high (see Equation 3.22). Hence, we expect a lower response when using a tighter photon selection since di-jet events are removed.

Since the "photon" energy in di-jet events will be measured too low, we also expect that E' will be underestimated. This means that the measured jet energy (of the correctly identified jet) will be greater in relation to E' in di-jet events. We therefore expect the measured jet energy of the E'-bins to decrease when di-jet events are removed.

The jet response was re-measured with five different `hmx7` criteria, `hmx7` < 6, 8, 12, 16 and 20. Results are shown in Figure 6.5. The effects discussed above can clearly be seen. The jet response decreases and the measured jet energy moves towards lower values when the photon criteria are tighten. The `hmx7` < 20 curve is 1% above our standard response curve at 40 GeV while the `hmx7` < 6 curve is more than 1% lower. The fractional difference

between the response fits in each cryostat can be seen as a function of measured jet energy in Figure 6.6.

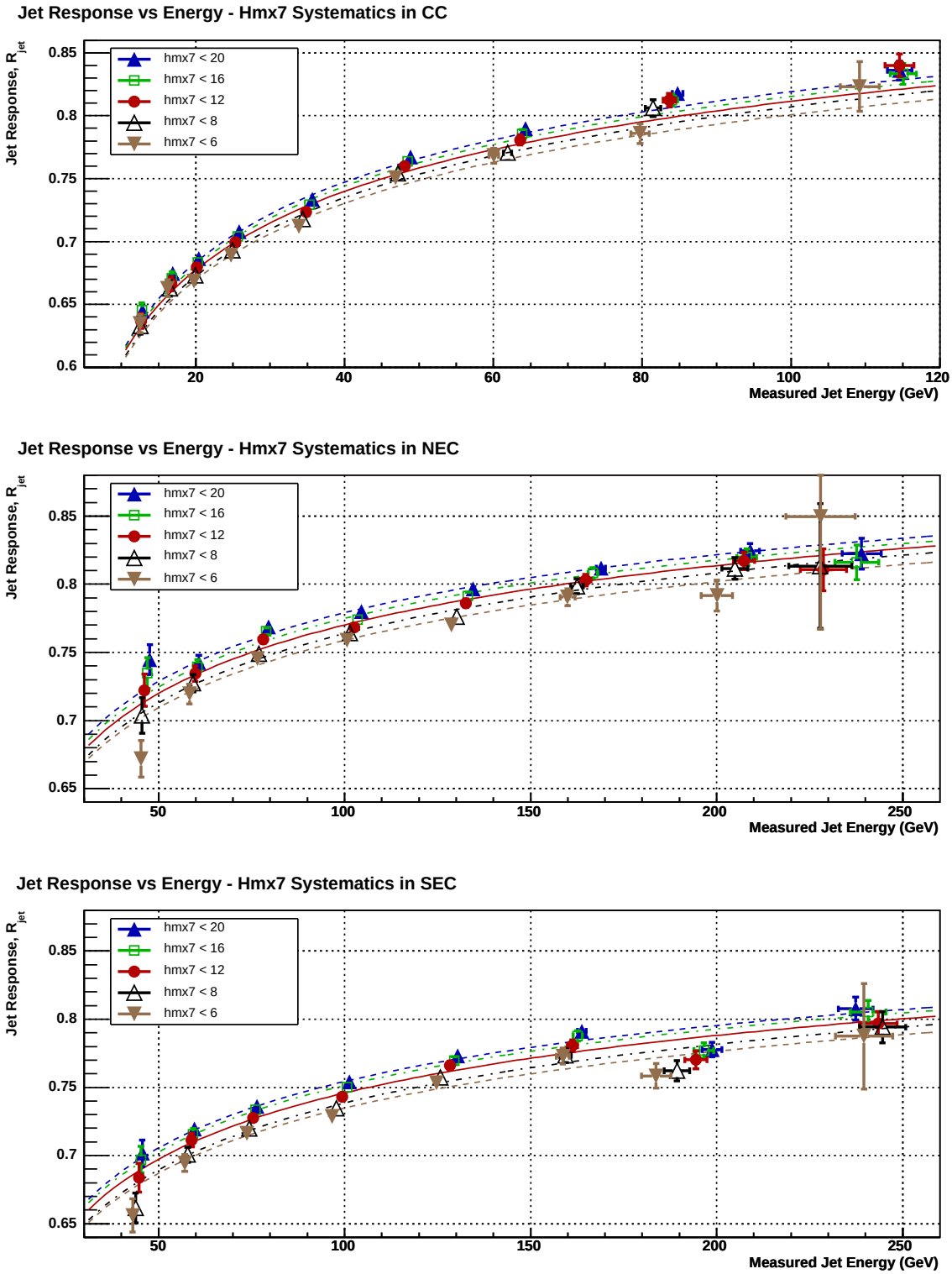

Figure 6.5: Jet response for jets in the different cryostats for five datasets using different H-matrix (photon identification) criteria. Tighter H-matrix criteria give lower jet response.

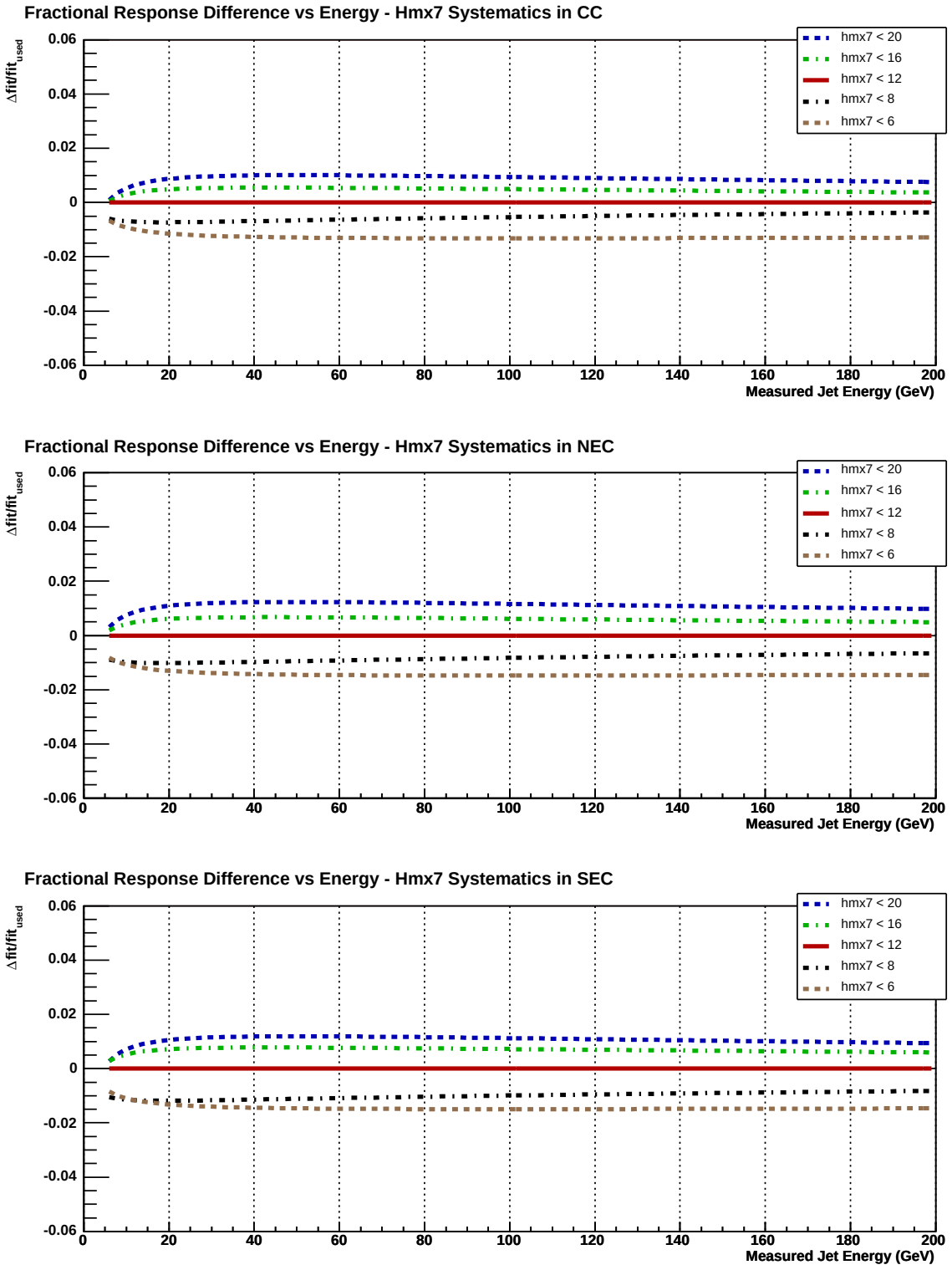

Figure 6.6: Fractional difference of the response fits of Figure 6.5. Tighter H-matrix criteria give lower jet response.

Photon η Systematics

In a perfectly pure direct photon sample with perfectly calibrated EM scale, our response measurement should be independent of the pseudorapidity of the photon. However, different contributions from background are expected depending on which cryostat the photon is in [5]. To study this, the jet response was determined separately for events when the photon was in the central calorimeter ($|\eta_\gamma^{det}| < 1.0$) and in each of the forward calorimeters (with borders $\eta_\gamma^{det} = \pm 1.6$ and $\eta_\gamma^{det} = \pm 2.5$). The results are shown in Figure 6.7.

The jet response in the CC is measured about 1% higher in events in which the photon is in the CC,[1] and about 3% lower when the photon is in any of the ECs as can be seen in Figure 6.8. The jet response in the ECs is even more sensitive to the photon η. Here we see response shifts up to 4%.

This shift could be explained by an inaccurate EM scale. If photons in the ECs would be assigned too high energies, our response would be measured too low when the photon is in any of the ECs (which is what we see). A more likely explanation is different contamination from di-jet events. For a given jet E_T, a jet in the EC (at $\eta = 2$) will have approximately 4 times the energy of a jet in the CC (at $\eta = 0$). Jets reconstructed as photons will hence usually have a higher measured energy in the ECs, even after cryostat corrections are taken into account. A higher "photon" energy means a lower response, which explains the shift.

If the latter scenario is true, this indicates that a large fraction of our $\gamma + jet$ events actually are di-jet events. In this case, the shift should decrease with better photon identification.

[1] The cryostats borders are defined differently for photons and jets, see Sections 4.3.4 and 4.3.8

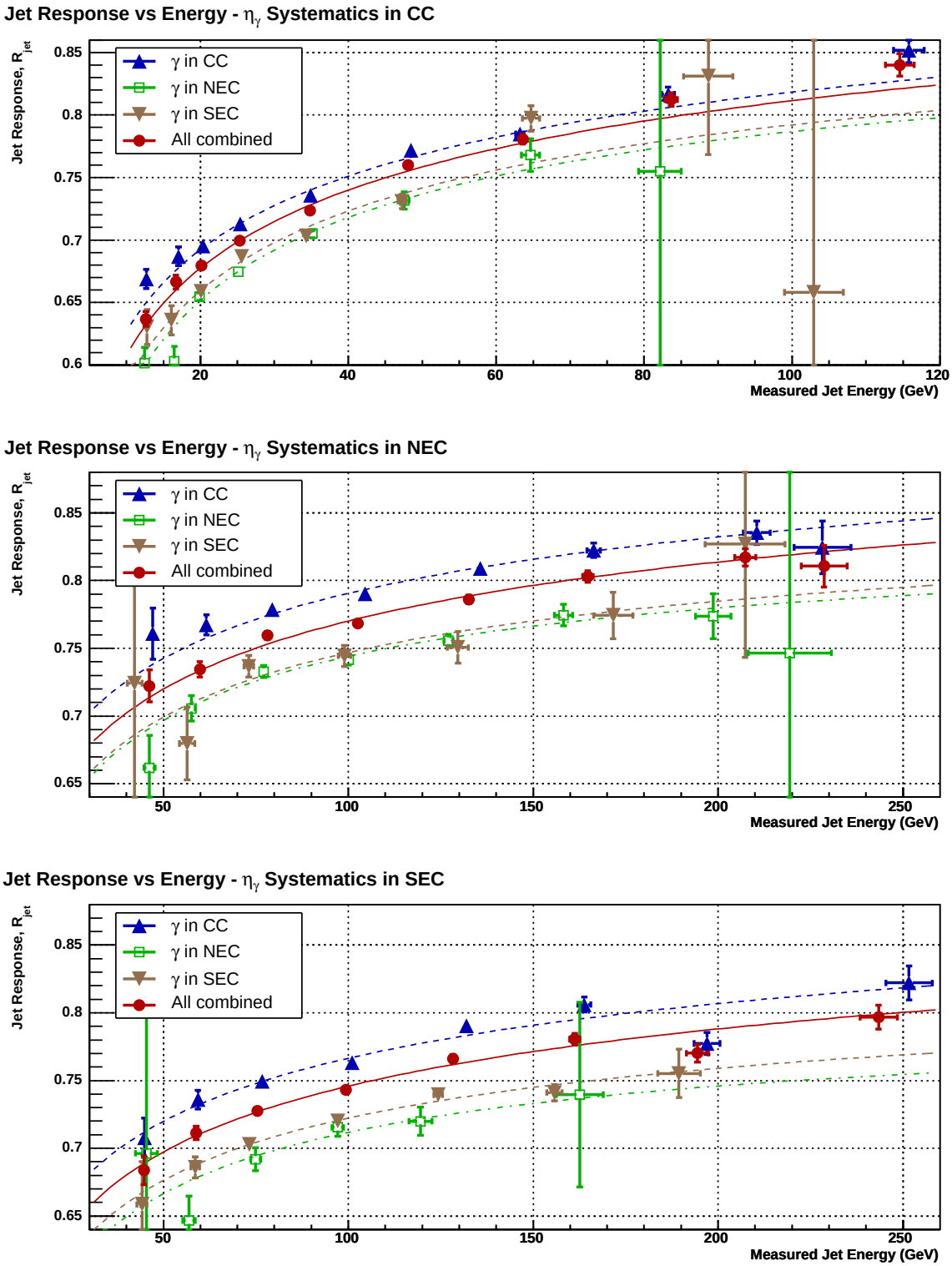

Figure 6.7: Our data sample was divided in three sub-samples depending on which cryostat the photon was in. The upper graph shows the jet response in the CC for different locations of the photon. When the photon is also in the CC, the response is measured higher. The lower two graphs show the jet response in the end caps for different photon locations. Here we still see a higher response when the photon is in the CC.

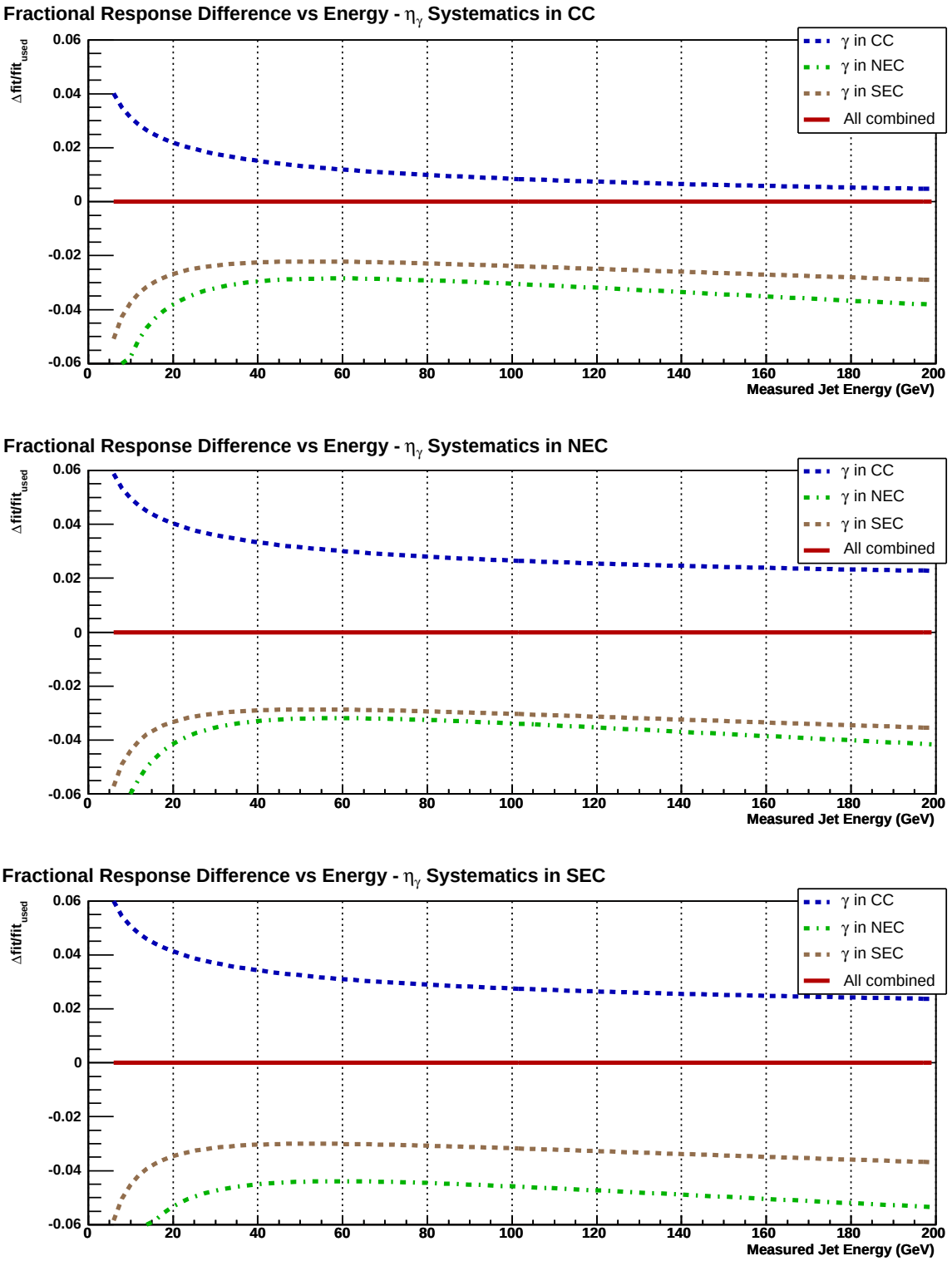

Figure 6.8: Fractional jet response difference depending on in which cryostat photon is. The lowest plot, which shows the jet response in the South end cap, is most sensitive to the location of the photon. Notice that the scale on the y-axis is different.

6.3 Back-to-Back Systematics

Previous studies have shown that the measured response curves in the different cryostats only take the same shape in case of a very tight back-to-back criterion between the photon and the jet [5].

In a leading order $\gamma + jet$ process, we can consider the final state parton as the recoil of the photon. After hadronization the produced jet will be back-to-back with the photon in the transverse plane, *i.e.* the azimuthal angle between the two objects will be: $\Delta\phi \sim \pi$. Due to calorimeter resolution effects and jet algorithm limitations, the reconstructed jet momentum vector will be different from the momentum vector of the particle level jet, and the jet will not be strictly back-to-back with the photon. There are also several next-to-leading-order processes where the hadronic recoil consists of two partons, *e.g.* if the produced parton radiates a gluon that hadronizes into a second jet. When this happens, the leading jet will be deflected. Because of these effects we generally expect a lower response when we loosen the back-to-back criterion.

In order to examine systematic effects of the back-to-back selection, the response was re-measured using four different $\Delta\phi$ criteria. The used were $\Delta\phi > 2.8$, 2.9, 3.0 and 3.1. The results are shown in Figure 6.9. No significantly better consistency of the response shape is seen between the samples. The response measurement in the low E_T-region seems somewhat better in case of the tightest back-to-back selection, but this improvement (if any) is very small. The reason for using the very tight $\Delta\phi > 3.1$ as the standard selection was rather to keep consistency with previous analyses.

This is the opposite effect to what was observed in Section 6.2. A tighter photon selection gives a lower response and lower jet energies in a given E'-bin. A tighter back-to-back selection generally gives a higher jet response and higher jet energies.

In Figure 6.9 the fractional response difference is shown between our standard $\Delta\phi > 3.1$ selection and the other back-to-back selections. The difference becomes larger at high energies.

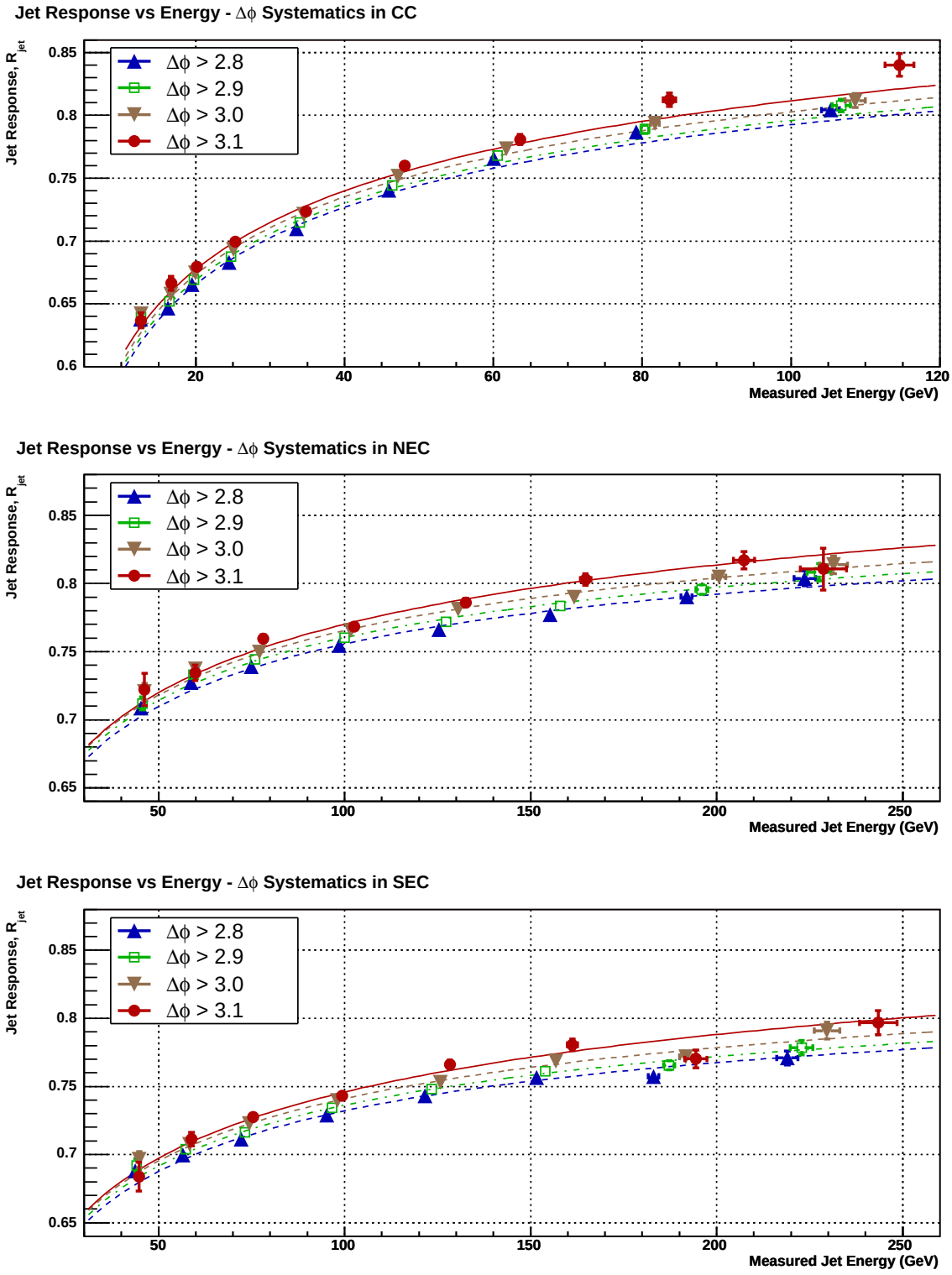

Figure 6.9: Jet response measured in the different cryostats for different back-to-back criteria. A tighter back-to-back selection gives a higher response.

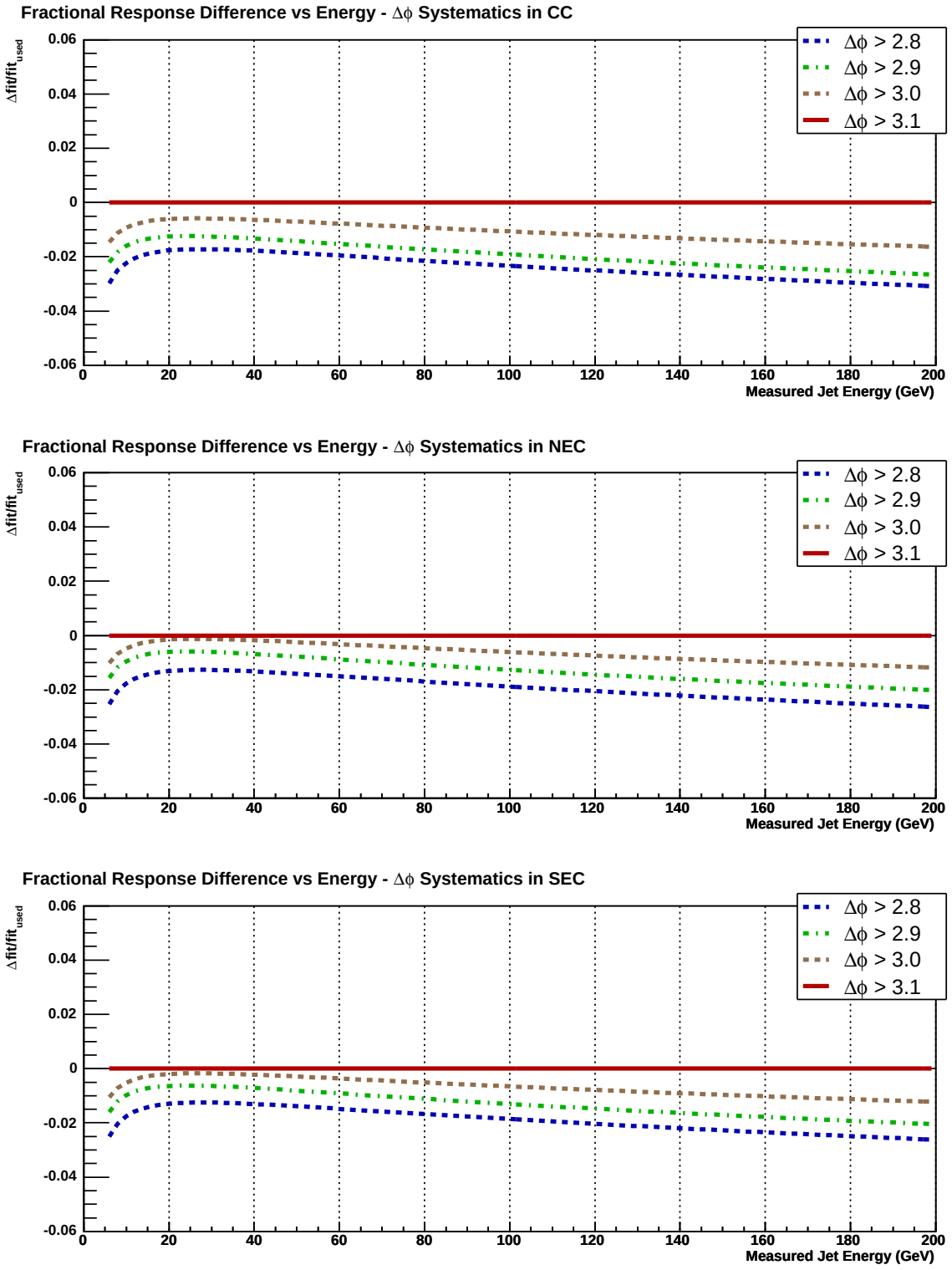

Figure 6.10: Fractional response difference for different back-to-back criteria. Notice that the difference keeps growing as energy increases.

Chapter 7

Summary

The DØ detector is currently recording data from $p\overline{p}$ collisions at $\sqrt{s} = 1.96$ TeV – the world's highest particle collision energies. The dominant physics process at these energies is jet production. Many analyses performed at DØ study processes where one or more jets are produced. An example of such a process is top quark production.

Data has been recorded at DØ at an increasing pace since 2001. As more data is recorded, the statistical uncertainties on our measurements decrease and systematic effects become more prominent. Jet Energy Scale is the dominant systematic uncertainty for many analyses, including top quark measurements.

The jet response is the most important contribution to the Jet Energy Scale. The jet response uncertainty is especially large for jets with measured transverse momentum below 25 GeV since the measurement of these jets is biased by the jet p_T reconstruction threshold. Until now, the jet response in this low E_T region has been obtained through extrapolating the measured response from higher energies, which is the main reason for the large uncertainties. In this study we improve the jet response precision for jets in this low E_T region.

The jet response was measured in $\gamma + jet$ events by applying the Missing E_T Projection Fraction Method to data recorded in the period April 2002 – August 2003 (the so-called PASS1 p14 dataset). In order to improve the response measurement precision at low E_T, the jet p_T reconstruction threshold was lowered from the standard 8 GeV to 3 GeV.

The measured response compares well with the official results implemented in `jetcorr 5.3`, where the response was measured in data from the same time period as the data used in this analysis. The response measurement reach at low E_T is extended from 20

to 12 GeV in the central calorimeter, and from 80 to 45 GeV in the end caps. This will lead to a significant improvement in our energy calibration of low E_T jets.

Using the lower jet threshold resulted in many new low p_T jets being found. This lower threshold has however no or very little effect on the reconstruction of jets with measured p_T above 12 GeV. For this reason we believe it is safe to apply these results to jets used in standard DØ analyses.

Bibliography

[1] Gregory Arhtur Davis, *First Measurement of the Differential Inclusive Cross Section for Jet Production at DØ Run II* FERMILAB-THESIS-2004-02, Dissertation, February 2004.

[2] Brad Abbot *et al.*, *Jet Energy Scale at DØ*, DØ Note 3287, August 1997.

[3] Brad Abbot *et al.*, (DØ Collaboration), *Determination of the Absolute Jet Energy Scale in the DØ Calorimeters*, November 1998.

[4] Robert Kehoe, *Search for the Top Quark in Dielectron Final States at* $\sqrt{s} = 1.8$ *TeV and Measurement of the Response of the DØ U/LAr Calorimeter to Jets*, FERMILAB-THESIS-1997-34, Dissertation, January 1997.

[5] Alexander Kupčo, *Jet Response for p14 Data and Monte Carlo*, Unpublished.

[6] Jonathan Kotcher, *Design, performance and upgrade of the DØ calorimeter*, FERMILAB-CONF-95-007-E January 1995.

[7] Richard Wigmans, *On the Energy Resolution of Uranium and Other Hadron Calorimeters*, Nuclear Instruments and Methods in Physics Research, A259:389-489, 1987.

[8] Dugan O'Neil, *Performance of the HEC and the Physics of Electroweak Top Quark Production at Atlas*, Nuclear Instruments and Methods in Physics Research, A338:386-347, 1994.

[9] Gerald Blazey, *Run II Jet Physics*, DØ Note 3750, April 2000.

[10] Emmanuel Busato & Bernard Andrieu, *Jet Algorithms in the DØ Run II Software: Description and User's Guide*, DØ Note 4457, August 2004.

[11] Bob Olivier, Ursula Bassler, Gregorio Bernardi, *NADA: A New Event by Event Hot Cell Killer*, DØ Note 3687, July 2000.

[12] Jean-Roch Vlimant, Ursula Bassler, Gregorio Bernardi, Sophie Trincaz-Duvoid, *Technical description of the T42 algorithm for the calorimeter noise suppression*, DØ Note 4146, May 2003.

[13] Gregorio Bernardi, Emmanuel Busato and Jean-Roch Vlimant, *Improvements from the T42 Algorithm on Calorimeter Objects Reconstruction*, DØ Note 4335, January 2004.

[14] Maxim Alexeev *et al.*, *Isolated jets in $\gamma + jet$ Run II DØ data and their application for JES settings*, DØ Note 4313, December 2003.

[15] Junjie Zhu, *Determination of Electron Energy Scale and Energy Resolution using p14 $Z^0 \to e^+e^-$ data*, DØ Note 4323, January 2003.

[16] Marcel Demarteau *et al.*, *Measurement of the W mass*, DØ Note 2929, April 1996.

[17] Ian Adam *et al.*, *Observation of $J/\psi \to ee$ decays at DØ and calibration of the central calorimeter electromagnetic energy scale*, DØ Note 2298, October 1994.

[18] Ulrich Heintz, *A Measurement of the Calorimeter Response Using π^0 Decays*, DØ Note 2268, August 1994.

[19] Robert Kehoe, *Resolution Bias in Jet Response Measurement*, DØ Note 2052, February 1994.

[20] *Common Sample Group, Main Page*, `http://www-d0.fnal.gov/Run2Physics/cs/index.html`, October 2004.

[21] *The top_analyze Package, version Stradivarius*, `http://www-d0.fnal.gov/Run2Physics/top/d0_private/wg/top_analyze/Stradivarius/Stradivarius.html`, May 2004.

[22] *Calorimeter Data Quality Page*, `http://d0-france.in2p3.fr/WORKING_GROUPS/DQ/`, July 2004.

[23] Ariel Schwartzman & Meenakshi Narain, *Probabilistic Primary Vertex Selection*, DØ Note 4042, November 2002.

[24] Mikko Voutilainen & Vivian O'Dell, *Measurement of Jet Response in the Inter Cryostat Region in p14 data*, Unpublished.